Status and future development of Heating and Current Drive for the EU DEMO

Original
Status and future development of Heating and Current Drive for the EU DEMO / Tran, M.Q., Agostinetti, P., Aiello, G., Avramidis, K., Baiocchi, B., Barbisan, M., Bobkov, V., Briefi, S., Bruschi, A., Chavan, R., Chelis, I., Day, Ch., Delogu, R., Ell, B., Fanale, F., Fassina, A., Fantz, U., Faugel, H., Figini, L., Fiorucci, D., et al.. - In: FUSION ENGINEERING AND DESIGN. - ISSN 0920-3796. - ELETTRONICO. - 180:(2022), p. 113159. [10.1016/j.fusengdes.2022.113159]

Publisher:
Elsevier Ltd

Published
DOI:10.1016/j.fusengdes.2022.113159

Fusion Engineering and Design 180 (2022) 113159

Contents lists available at ScienceDirect

Fusion Engineering and Design

journal homepage: www.elsevier.com/locate/fusengdes

Status and future development of Heating and Current Drive for the EU DEMO

M.Q. Tran [a], P. Agostinetti [b], G. Aiello [c], K. Avramidis [d], B. Baiocchi [e], M. Barbisan [b], V. Bobkov [f,n], S. Briefi [f], A. Bruschi [e], R. Chavan [a], I. Chelis [g], Ch. Day [h], R. Delogu [b], B. Ell [d], F. Fanale [e], A. Fassina [b], U. Fantz [f], H. Faugel [f], L. Figini [e], D. Fiorucci [b], R. Friedl [i], Th. Franke [f,j], G. Gantenbein [d], S. Garavaglia [e], G. Granucci [e], S. Hanke [h], J.-P. Hogge [a], C. Hopf [f], A. Kostic [f], S. Illy [d], Z. Ioannidis [d], J. Jelonnek [d], J. Jin [d], G. Latsas [g], F. Louche [k], V. Maquet [k], R. Maggiora [l], A. Messiaen [k], D. Milanesio [l], A. Mimo [f], A. Moro [e], R. Ochoukov [f], J. Ongena [k], I.G. Pagonakis [d], D. Peponis [g], A. Pimazzoni [b], R. Ragona [k], N. Rispoli [e], T. Ruess [d], T. Rzesnicki [d], T. Scherer [c], P. Spaeh [c], G. Starnella [f], D. Strauss [c], M. Thumm [d], W. Tierens [f], I. Tigelis [g], C. Tsironis [m], M. Usoltceva [f], D. Van Eester [k], F. Veronese [b], P. Vincenzi [b], F. Wagner [m], C. Wu [d], F. Zeus [f], W. Zhang [f], Contributors from all Laboratories which have contributed to the Work Package HCD during 2014-2020

[a] *Ecole Polytechnique Fédérale de Lausanne (EPFL), Swiss Plasma Center (SPC), Station 13, Lausanne, 1015, Switzerland*
[b] *Consorzio RFX (CNR, ENEA, INFN, Università di Padova, Acciaierie Venete SpA, Corso Stati Uniti 4, Padova, I-35127, Italy*
[c] *IAM-AWP, Karlsruhe Institute of Technology (KIT), Kaiserstr. 12, Karlsruhe, 76131, Germany*
[d] *IHM, Karlsruhe Institute of Technology (KIT), Kaiserstr. 12, Karlsruhe, 76131, Germany*
[e] *Institute for Plasma Science and Technology, National Research Council (ISTP-CNR), via Cozzi 53, Milan, 20125, Italy*
[f] *Max Planck Institute for Plasma Physics, Boltzmann Strasse 2, Garching, 85748, Germany*
[g] *National and Kapodistrian University of Athens, Department of Physics, Zografou, Athens, GR-157 84, Greece*
[h] *ITEP, Karlsruhe Institute of Technology (KIT), Campus North, Hermann-von-Helmholtz-Platz 1, Eggenstein-Leopoldshafen, 76344, Germany*
[i] *AG Experimentelle Plasmaphysik, Universitt Augsburg, Augsburg, 86135, Germany*
[j] *EUROfusion Consortium, Boltzmannstr. 2, Garching, 85748, Germany*
[k] *LPP-ERM/KMS, Laboratory for Plasma Physics, Royal Military Academy, TEC Partner, Renaissancelaan 30, Brussels, 1000, Belgium*
[l] *Politecnico di Torino, Corso Duca degli Abruzzi 24, Torino, 10129, Italy*
[m] *National Technical University of Athens, School of Electrical and Computer Engineering, Zografou, Athens, GR-157 71, Greece*
[n] *Max Planck Institute for Plasma Physics, Wendelsteinstrasse 1, Greifswald, 17491, Germany*

ARTICLE INFO

Keywords:
Heating
Current Drive
Electron Cyclotron
Ion Cyclotron
Neutral Beam
DEMO

MSC:
0000
1111

PACS:
0000
1111

ABSTRACT

The European DEMO is a pulsed device with pulse length of 2 hours. The functions devoted to the heating and current drive system are: plasma breakdown, plasma ramp-up to the flat-top where fusion reactions occur, the control of the plasma during the flat-top phase, and finally the plasma ramp-down. The EU-DEMO project was in a Pre-Concept Design Phase during 2014-2020, meaning that in some cases, the design values of the device and the precise requirements from the physics point of view were not yet frozen. A total of 130 MW was considered for the all phases of the plasma: in the flat top, 30 MW is required for neoclassical tearing modes (NTM) control, 30 MW for burn control, and 70 MW for the control of thermal instability (TI), without any specific functions requested from each system, Electron Cyclotron (EC), Ion Cyclotron (IC), or Neutral Beam (NB) Injection. At the beginning of 2020, a strategic decision was taken, to consider EC as the baseline for the next phase (in 2021 and beyond). R&D on IC and NB will be risk mitigation measures. In parallel with progresses in Physics modelling, a decision point on the heating strategy will be taken by 2024. This paper describes the status of the R&D development during the period 2014-2020. It assumes that the 3 systems EC, IC and NB will be needed. For integration studies, they are assumed to be implemented at a power level of at least 50 MW. This paper describes in detail the status reached by the EC, IC and NB at the end of 2020. It will be used in the future for further

https://doi.org/10.1016/j.fusengdes.2022.113159
Received 15 October 2021; Received in revised form 11 April 2022; Accepted 25 April 2022

development of the baseline heating method EC, and serves as starting point to further develop IC and NB in areas needed for these systems to be considered for DEMO.

1. Introduction

Heating and Current Drive (HCD) is a key component for a successful operation of DEMO and is the objet of dedicated work package: WPHCD (Work Package on Heating and Current Drive). In the present (2020) design, the main functions foreseen for the HCD system encompass the plasma breakdown, the plasma ramp-up (including the L to H transition, with a power level of about 130 MW) and, if necessary, the heat to burn assistance through the power deposition on ions to increase the ion temperature for fusion reactions production, the control of the plasma during the flat-top phases: 30 MW for bulk heating (BH), 30 MW for control of MHD modes, in particular NTMs at the $q= 3/2$ and 2/1 surfaces, and 70 MW for Thermal Instability (TI) control with a power deposition at $\rho > 0.9$, and finally the assistance to plasma ramp-down. The version considered in the programme is a “pulsed DEMO” with a pulse duration of 2 hours. No CD requirement is foreseen except for the control of NTM modes.

During the period 2014-2020, the EU-DEMO project was in a Pre-Concept Design Phase, meaning that in some cases, the design values of the device and the precise requirements from physics point of view were not yet frozen: the above outline of power requirements were given at the end of 2019. In particular, there was no clear definition of the role for each potential heating system (by Electron Cyclotron (EC), Ion Cyclotron (IC) waves or by Neutral Beam (NB) injection) and the possible heating mix(es). The original strategy was to develop all three heating methods up to a level sufficient for assessing, in 2024, their potentialities based on physics requirements and on their Technological Readiness Level (TRL). Since the programme did not have any indication of the required heating mixes, it was decided to develop all three systems at a power level of 50 MW. This development includes R&D on the sources, the transmission lines and the launchers/antennas and, as much as possible, the various integration aspects (such as neutronics loads and remote maintenance).

At the beginning of 2020, an important strategic decision was taken by the DEMO leadership. The programme in 2021 and beyond will be focused and EC will be the heating baseline. The two other heating methods will be developed in the frame of a risk mitigation approach, with a decision point by 2024, taking into account the scenarios developed by physics and the need to heat ions.

This paper describes the results obtained on EC (section 2), IC (section 3) and NB (section 4) until the end of 2020. Pursuing the original strategy, each system was developed for a power deposited to plasma in the range of 30-50 MW. This power level is high enough to assess the requirements on the number of ports (MW/ports), reliability issues (which will impact the number of ports), as well as realistic implementation studies.

The physics basis for Heating and Current Drive in DEMO is given in ref. [1]. For EC, the specific functions are the plasma breakdown, the control of NTMs and the TI control. Naturally EC can also deposit power either in the plasma bulk or core, as required by physics. With the definition of the requirements at the end of 2019-beginning of 2020, the EC system is designed for a deposited power of 130 MW at different positions in the plasma. The NTM control requires the deposition of the power at a precise location ($q = 3/2$ and $q = 2/1$). For this, two variants were developed: the Variant at Fixed Frequency (Variant FF) uses gyrotrons able to operate at pairs of fixed frequencies (136/170 GHz or 170/204 GHz) and a steerable mirror to deposit the power at the desired q surfaces. The R&D focuses on 2 MW coaxial gyrotrons capable of operation at two or more frequencies. For the Variant Tunable Frequency (Variant TF) the deposition at the desired q surfaces is achieved by tuning the gyrotron frequencies in a ±10 GHz range in steps of 2-3 GHz to match the local magnetic field along a fixed line of sight. For this Variant, a very promising development of large diamond windows was undertaken, leading to the production of 180 mm diameter disc, to be used in a Brewster window arrangement. The study also includes a first assessment of the impact of reliability on the total installed power to reach the required power to plasma, assuming a reliability of 0.999.

For the IC system, the design indicates the feasibility of straps antenna with sufficient power per antenna. The IC heating also satisfies physics requirements (ion heating, minimization of impurity production and of parasitic power absorption) which are described in the paper.

Compared to 2014, the NB design was reoriented to best benefit from the return of experience (RoX) from the ITER Neutral Beam system. The R&D was very broad and encompasses technology for DEMO use (such as Cs management and RF racetrack drivers) and methods to increase the efficiency by improving the neutralisation (the “Beam Driven Plasma Neutralizer”) or the photoneutralization (in view of a post-DEMO device).

2. Electron Cyclotron Heating System

The Electron Cyclotron (EC) system is in charge of key functions including initiating, sustaining and assisting the tokamak plasma discharge as mentioned before. With the possible exception of the direct ion heating during the L to H transition and heat to burn phases, which at present has not yet been proven to be necessary, all present physics requirements for HCD systems can be met by the EC system, provided it is fed by a sufficient number of sources with a sufficient number of injection ports to ensure high reliability. At present, two or three injection frequencies, and up to six equatorial ports are envisaged to accomplish all tasks. The physics requirements indicate the need for a large amount of power, with a power deposition region spanning the plasma radius from the centre to the edge, and hence with different local magnetic fields. This cannot be obtained with a single injected frequency unless an unrealistic wide injection angle is used, implying the use of unacceptably wide apertures in the breeding blanket (BB). The number of ports to be used is linked to the use of spare gyrotrons needed to guarantee a very high system reliability required by the DEMO plant.

The development of the Pre-Concept Design (PCD) Phase of the DEMO EC system was substantial. The preliminary evaluations in terms of CD efficiency have been revised and a complete system design has been realised, tailored on an initial set of requirements, both from physics (in terms of required injected power, location and driven current for NTM control) and from engineering sides (mainly neutron and radiation loads). All main issues were addressed and the system developed considering plasma baseline scenarios which evolved during the design phase. This required adaptation of the system, mainly affecting the required injection wave frequency and angles, consisted of adjusting of launcher optics and design of the gyrotron sources. To satisfy the requirements, a set of antenna options (including open- ended waveguides (WGs) and Remote-Steering antennas) have been investigated. These solutions were actually discarded due to low focusing capability, and were replaced by a launcher design with focusing mirrors at the end of 2019, which was refined in 2020 to include the latest physics requirements.

The system will be described in the following sections, starting from the launcher, the subsystem that is the most sensitive to the requests of physics. Other sections will deal with the Transmission Line (TL) description in and outside the nuclear building and finally with the gyrotron sources. The present requirements from physics are found in the document HCD System Design Requirements (SRD) [2].

2.1. EC optical system and launcher design

For all design and R&D, the gyrotron power is assumed to be 2 MW. The EC launcher design consists of optical and mechanical parts. The optical design (defining the propagation direction and size of the microwave beams) is mainly driven by the key functions assigned to the EC system by the SRD with the position of the mirrors, subject to additional constraints, such as electromagnetic and nuclear loads. The mechanical design, bounded by the physical constraints of beam envelopes, is conditioned by space limitations, radiation induced material degradation, radiation shielding, cooling and heat transport, and Remote Handling (RH) needs.

Optimal launching directions were obtained by analyses performed with the Beam-Tracing codes TORBEAM [3] and GRAY [4]. Based on multi-parameter ray-tracing tables (poloidal and toroidal injection angles, wave frequency), the location in radial coordinates and the driven current were determined for any combination of parameters [5].

Different launching points in the equatorial port (EP) and from positions corresponding to a possible port location in intermediate positions between the Equatorial and the Top DEMO ports were used for the analyses using the 2018 baseline [6]. The gyrotron frequencies of 170 and 204 GHz, compatible with the use of a window with minimal reflection at the two frequencies were assumed for the analysis (Fig. 1). Poloidal (α) and toroidal (β) launching angles are chosen in the NTM case minimizing the deposition width and maximizing the driven current at the NTM location. The need to move the deposition location to follow the NTM magnetic island during the various phases of the discharge required the development of two possible configurations for the EC system. The change in the deposition location is obtained in the FF Variant [7] by varying the launching angle with mechanical steering at fixed frequency. However, a mechanical mirror steering mechanism placed close to the plasma is exposed to very high radiation loads and neutron induced material degradation. In theTunable Frequency (TF) option [8] the deposition location may be varied by changing the injected wave frequency while launching from a fixed mirror. For these two configurations, a single launcher has been devised, with the difference that in the case of the FF option, steerable front mirrors would be used for NTM stabilization instead of fixed mirrors.

The EC launcher has been designed at first with two different types of antennas aiming at the two main specific radial locations required by NTM stabilization ($0.6 < \rho < 0.8$, see Fig. 2, left) and BH (plasma centre, $\rho < 0.3$, Fig. 2, right) while heating at plasma edge for TI control can be realized by changing the injection frequency of the wave, using the same angular injection as for the BH [9].

In case of NTMs the beam convergence has been adapted to the need for a small deposition region (6 cm full-width at $1/e$ of the CD profile), using the largest possible focusing steering mirrors (SMs). The effect of possible beam broadening due to turbulence is not included in the present design [10]. For BH and TI control, the requirement of convergence is much less stringent, so that smaller fixed focusing mirrors (FMs) can be used. The number of beams on each mirror is balanced considering the power required for the task, the number of lines compatible with the mirror size, the space available at the back of the port for the WG vacuum feed-throughs and the space occupation outside the port.

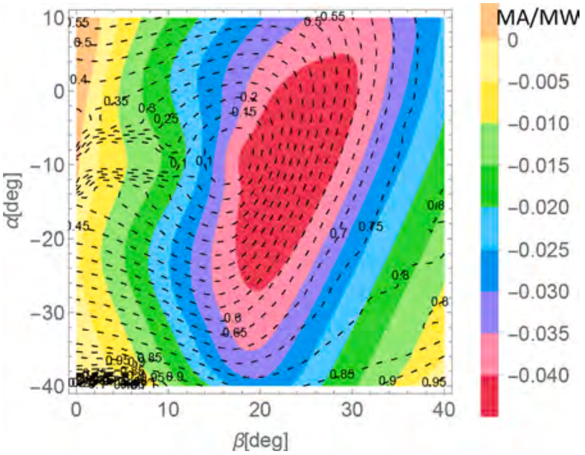

Fig. 1. Contour plot showing the normalized deposition location ρ (black dashed curves) and total driven current ICD (in color, in MA/MW) as a function of the injection angles (α, β) at 170 GHz.

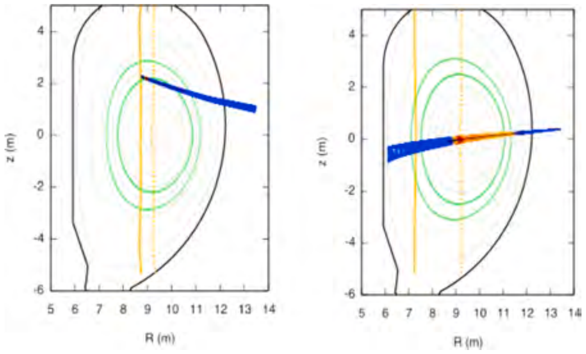

Fig. 2. Computed sections of the DEMO plasma flux surfaces together with the beam paths (in blue) and the resonance locations (in orange the “cold plasma” resonance and in light orange the “hot plasma” one), determining different power deposition localization by the different crossing position. Trajectories are bent by refraction in the dense plasma and beams are chosen converging (for NTMs) and diverging (for BH). Surfaces where the NTM instabilities are located are shown in green. Absorption occurs when the blue beams change color to red.

Each launcher unit, located in the equatorial port, holds 4 mirror antennas with a total of 22 beam-lines [11], in both FF and TF variants. Two NTM mirrors are located at the top and bottom of the equatorial port (EP), reflecting 3 beams each, aiming upwards and downwards at the upper $q = 3/2$ and lower $q = 2/1$ NTM positions (in Fig. 3 the central and extreme positions for the mirrors, are shown in light blue, green and magenta) in the case of the FF variant. For the TF variant, the

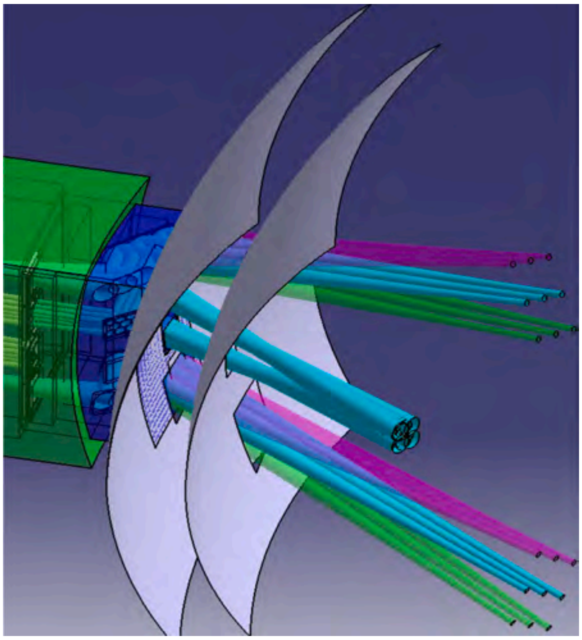

Fig. 3. Layout of the launcher in the equatorial port, with beam trajectories and envelopes represented by blue, green and magenta envelopes at top and bottom for NTM control and in light blue at centre for BH and RI control.

mirror is fixed in one position and the launched beam frequency is tuned. For BH and TI control two Multi-Beam Mirror (MBM) antennas, common to the FF and TF variants are used, carrying 8 beams each, located close to the equatorial mid plane and aiming at the plasma centre. The launch direction is such as to provide co-driven current (co-CD), following the definition of the magnetic field and current directions [12].

The beams are launched from the opening of a corrugated WG in the port interior, and converted from the HE_{11} mode to a Gaussian beam (TEM_{00} mode) with an efficiency higher than 98% (that can be increased with a HE_{11}-to-TEM_{00} converter). They are reflected on two metallic mirrors, M1 and M2 which refocus the expanding beams in the port front area, before reaching the plasma. MBMs are used for reducing the mirror area, as one mirror carries more beams overlapping on the mirror surface. While the dogleg shaped beam path protects from the direct streaming of neutrons through the WGs, the proposed layout is compatible with the realisation of two separate launcher submodules, one for M1-type and the second for M2-type mirrors. When mirror maintenance or replacement is required for the plasma facing mirror M2, this arrangement allows the extraction of the corresponding module while leaving the other in place. With the same aim, all the WGs run on one side of the port, leaving room for the extraction of the section housing the launching mirrors (M2), without removing the WGs (see next section). The launcher was analysed for neutron and plasma radiation loading. A summary of the loads can be found in [13].

The mirror sterring mechanism is a crucial subsystem in the Variant FF. It has been the subject of specific studies, starting from the experience gained with the design of the ITER steering mirror mechanism. The main differences are the much larger size of the NTM antenna in DEMO and the position of the actuator, foreseen behind the mirror for space limitations and better shielding, instead of being on the mirror side, on the rotation axis. The PCD foresees a mechanism located on the mirror back side, based on the kinematic principle of a pantograph [14], which keeps the mirror rotation axis on the mirror surface, as required for minimising space occupancy and optical aberration, without need for mechanical elements on the mirror axis. Cooling spirals are foreseen at each joint, for proper cooling of the mirror and of each moving pantograph element (Fig. 4).

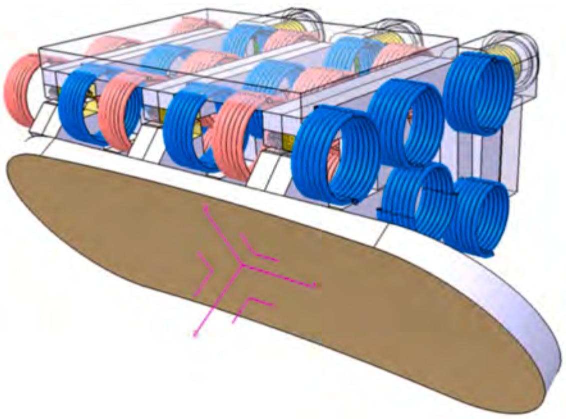

Fig. 4. View of the mirror M2 steering mechanism with cooling spirals (from [14]).

2.2. EC Optical system launcher integration

The EC optical system in-vessel components are integrated into the EC equatorial port plug (EPP) structural system [15]. The proposed design optimizes precise alignment, mechanical robustness, operational reliability and maintainability [16]. The mirrors are installed into the port plug modules either by flanges (fixed mirrors for NTM-control) or by integral blocks (all others), providing safe fastening and connectivity to supply systems (cooling, actuator gas, control). These concepts also allow maintenance after de-installation and transport of the port plug modules into the Active Maintenance Facility (AMF). The layouts for the NTM-control system and for the plasma heating system are respectively shown in Figs. 5 and 6.

At the rear side of the quasi-optical beam sections with mirrors, the microwave power is transmitted through WGs. Two bundles of three WGs each are installed for NTM-control and two bundles of eight WGs each provide power for BH and TI control.

The in-vessel WG bundles for NTM-control are installed at the top and the bottom region of each EC launcher. They have a length of up to three meters (starting from the vacuum side of the closure plate). They are arranged in a converging skewed position to each other with a total angle in between the WGs of ca. 4.6°.

This arrangement is justified by the need to have the smallest possible steering mirror (with overlapping of beam spots on M2), a s well as to achieve the proper collimation of the three “toroidally equivalent“ beams through the plasma. To avoid warping by thermal expansion, the NTM WGs are fastened by a fixed-loose support system where the fixed element is the closure plate sub-plate (CPSP) at the rear, mounted to the port closure plate (CP). The tips of the NTM WGs extend into the auxiliary shield blocks to avoid neutron streaming into the port, where a slide bearing vertically supports a frame that guarantees the precise position of the WG's at their front. The CPSP also provides connections for active water cooling of the WGs. The layout is shown in Fig. 7.

Fig. 8 shows the integration concept of the BH/TI control WG bundles. They are located in between the NTM-control WG bundles, closer to the horizontal mid-plane of DEMO. With a length of ca. 5 meters they protrude through individual openings of the auxiliary shield block A, and then terminate inside the FM EPP module. They are slightly oblique to each other (about 0.5° in toroidal direction and about 0.7° in poloidal direction) in order to converge on the mirrors and have the smallest possible mirror size (with partial overlapping of beam spots) minimizing also the opening in the BB.

The WGs are mounted with their rear end to feedthroughs on dedicated CPSPs. Together with slide bearings inside the FM EPP module, a fixed-loose support system is created. The WGs active cooling water supply is provided from the CPSPs.

2.3. EC Transmission line

The TL foreseen for the long path from the RF Building to the Nuclear Building (a minimum distance of 150 m is necessary for reduction of the tokamak stray field for a safe gyrotron operation) is partly in Quasi-Optical (QO) and partly in WG propagation. The longer part is constituted by a sequence of MBMs constituting a confocal QO TL, like in W7-X stellarator [17]. The line is arranged in a linear path with doglegs at each mirror unit [18], composed by a couple of mirrors (plane and focalising), all enclosed in cylindrical evacuated tubes.

In the RF building (see Fig. 9), where the gyrotrons will be located in

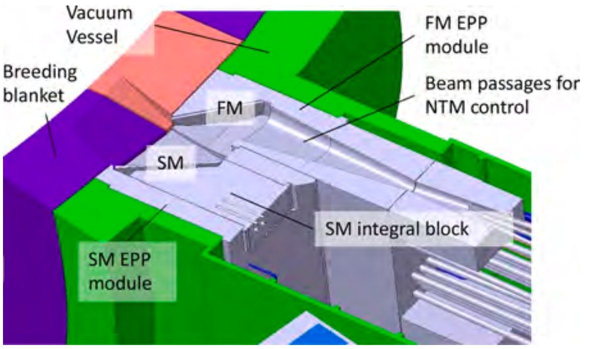

Fig. 5. Outline of the EC mirror integration concept for NTM-control.

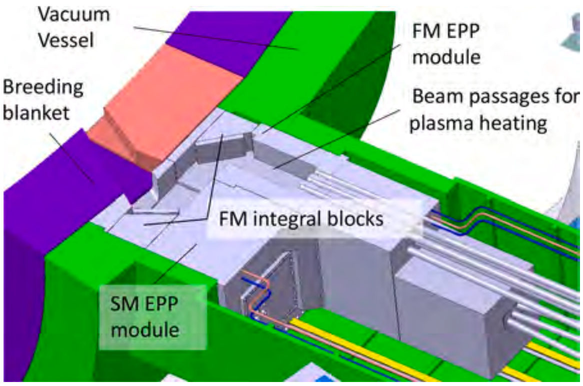

Fig. 6. Outline of the EC mirror integration concept for plasma heating.

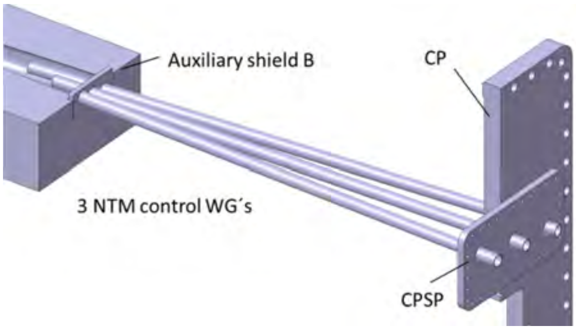

Fig. 7. Layout of the NTM-control in-vessel WGs integration concept.

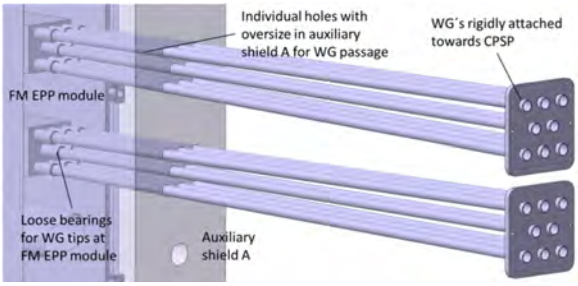

Fig. 8. Outline of the BH/TI in-vessel WGs integration concept.

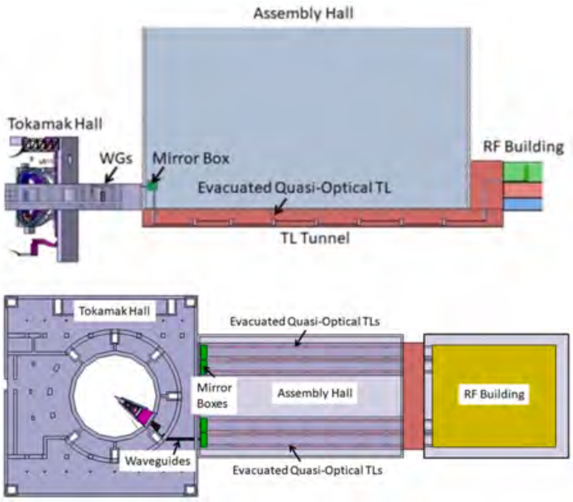

Fig. 9. Sketch of the routing of the TL from the Gyrotron Hall to the DEMO tokamak hall. Top: side-view, Bottom: top-view.

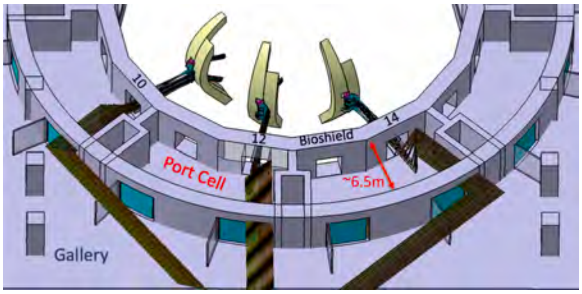

Fig. 10. Example of WG routing from the Assembly Hall to the port cell, with a minimal set of bends.

groups (corresponding to clusters), individual quasi-optical lines under vacuum will transmit single beams to a packed set of mirrors, where they will be combined to single beam bundles, one for each cluster. Each beam bundle will be directed as an independent QO line downward to pass through tunnels under the Assembly Hall, and then upward where they will terminate at the external part of the Nuclear Building wall, in a dedicated space into the Assembly Hall. Here the bundles are separated by a splitting mirror assembly, to be directed to the WG inputs, for the transmission of power in the Nuclear Building, through the gallery and in the port cell.

The EC TL inside the tokamak hall is constituted by a set of single WGs including mitre bends, a diamond RF window in the port cell and shutter valves, improving the availability of other lines in the same cluster in case of failure in one line. An example routing is shown in Fig. 10. Parallel WGs run close to the ceilings of the port cell and gallery of the 1st floor of the tokamak building and connect to the port flange at the equatorial level with a limited number of mitre bends. The occupation of space in front of the port has to be optimised to leave enough space to extract the SM port plug.

The tokamak RF window will be placed out of the axis of the WG entering the vessel, in order to protect it from the damages caused by direct neutron streaming. The use of a standard single-disk diamond RF window is foreseen for the FF variant of the system, with the advantage of the similarity with the gyrotron window, but capable to withstand possible vacuum vessel or WG overpressures. For the TF variant, a broadband Brewster-angle (see section 2.7) or alternatively a double-disk window with variable disk separation is needed, in order to minimise the reflection coefficient at multiple closer frequencies.

The TL losses are estimated to be in average approximatively 15% at all frequencies, considering corrugated HE_{11} aluminium WGs with 63.5 mm inner diameter in the Nuclear Building and QO TL outside.

2.4. *Number of gyrotrons and Reliability Studies*

The capability of the system to provide the required power is assured by installing a sufficient number of gyrotrons. The exact number to be installed, given a required system overall reliability and availability, will depend on realistic assumptions on the reliability of the different parts of the system and on the expected transmission losses, and will be part of future investigations. The study for the present launcher design with 22 beam-lines and 2 clusters per port, with the requirement of 30 MW for BH, 30 MW for NTMs and 70 MW for TI stabilization (30+30+70 option), has been detailed in [13]. A goal of a reliability higher than 99.9% for all tasks is satisfied with at least 5 full operative ports for the nominal gyrotron RF output power of 2 MW.

2.5. Verification and optimization of a 2 MW coaxial-cavity technology for DEMO

The worldwide effort in gyrotron development is described in [19–27]. Of particular importance is the R&D made for ITER, which requires the installation of 24 gyrotrons operating at 170 GHz and delivering 1 MW during 3600s. Considering the gyrotron development within EUROfusion, the major performance targets and the resulting development route towards a future DEMO gyrotron that were chosen for the period until 2020 are described in [28] and [29]. The major targets remain valid for the research period until 2025.

Table 1 shows the performance targets for DEMO in comparison with the specifications that were requested for the first installation in ITER. It shows the significant step forward in gyrotron R&D that is necessary to bridge the gap between today's state-of-the-art gyrotrons and future gyrotrons for DEMO. Significant challenges are posed by the need for moving from 1 MW to 2 MW output power, operation at multiple frequencies to allow for multi-purpose usage and reaching operating frequencies above 200 GHz. Although the total gyrotron efficiency target has been relaxed from 60% down to 50% for the coming research period (scoping studies for DEMO on efficiency show that there is no major benefit for >60%), the gyrotron efficiency remains a major concern for the total efficiency of the DEMO EC heating system. That is even more true if an operation at different frequencies is required. Another major requirement is the fast frequency tunability in steps of 2-3 GHz for TF Variant. Finally, the level of Reliability-Availability-Maintainability-Inspectability (RAMI) and advanced gyrotron control are major topics.

Two main design paths are known for high-power fusion gyrotrons: the conventional hollow-cavity design as used for instance for W7-X and ITER, and the coaxial-cavity design [19]. This latter concept was originally considered for the EU ITER gyrotron [30]. At the beginning of the former EUROfusion research period, detailed studies have proven that the coaxial-cavity concept is the most promising, if considering an output power of 2 MW and a frequency ≥ 170 GHz. The enhanced mode selectivity of a coaxial cavity permits stable operation on very high-order operating modes [31], which are compatible with a large cavity dimensions. It seems not possible to achieve these performance targets by using the conventional hollow-cavity design even if complex operation scenarios are considered [32]. Fig. 11 shows a 3D image of the European 170 GHz 2 MW coaxial-cavity gyrotron pre-prototype.

The 170 GHz 2 MW $TE_{34,19}$-mode modular-type short-pulse coaxial-cavity gyrotron pre-prototype at KIT has already exhibited excellent performance in pulses in the ms range [33]. The major step to prove the applicability of the coaxial-cavity gyrotron technology for DEMO is to demonstrate experimentally its capability of long-pulse (2 h) operation, especially with respect to the cooling and alignment of the coaxial insert. As it was not possible to build an industrial gyrotron due to limited budget yet, the short-pulse pre-prototype at KIT has been rebuilt and upgraded with new, water-cooled components [34]. First experiments targeting 50 ms pulses have been performed [35]. By implementing a long-pulse collector and a chemical vapour deposition (CVD)-diamond disk the pulse length shall be significantly increased above 100 ms. Advanced multi-physics simulations on the cooling of the insert have also been performed which proof theoretically the capability of the coaxial-cavity concept for a DEMO gyrotron [36,37]. In addition to the cooling of the insert, further improvements of the DEMO gyrotron have to be considered.:

Table 1
DEMO Gyrotron requirements for Variant FF with 3 frequencies and Variant TF with 3 frequencies plus frequency tuning versus ITER [29].

	EU DEMO	*ITER*
Frequency	(136)/170/204 GHz	170 GHz
Power	2 MW	1 MW
Efficiency	≥ 50 %	50 %
Tunability for TF Variant	±10 GHz (in steps of 2-3 GHz)	none
RAMI level	Power plant	Experimental

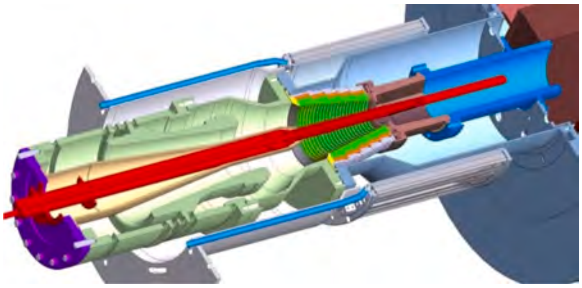

Fig. 11. 3D image of a typical coaxial insert (red) within a coaxial-cavity gyrotron [28].

- The maximum heat load on the cavity wall is one of the major limiting technological factors for the maximum achievable output power, and a very efficient cooling of this component is necessary. In this frame, different concepts are under theoretical and experimental investigation. They include the performance evaluation of a possible mini-channel cavity cooling system and the development of a mock-up test set-up for experimental validation [38].
- High-power gyrotrons may suffer from parasitic oscillations that are excited in the electron-beam compression zone. Different structures that reduce the possibility of parasitic excitation by increasing the starting currents of unwanted modes [39] are under consideration.
- Future advanced gyrotron operation requires mandatorily to improve the capabilities of the emitter and the electron optics. Considering the recent understanding of the physics of electron trapping mechanisms taking place in the Magnetron Injection Gun (MIG) region and the sensitivity of the electron beam quality to the emitter ring manufacturing tolerances, a MIG has been designed and manufactured that minimizes the influence of the manufacturing tolerances and misalignments on the quality of the generated electron beam. The design is optimized to generate a good beam quality in a wide variety of magnetic field profiles to increase the flexibility [40]. An additional important feature of the new triode MIG design is the possibility to operate with only two power supplies by using a special start-up scenario.

  In addition, a very promising Inverse Magnetron Injection Gun (IMIG) has been designed and built. Compared to conventional MIGs, it offers the possibility to implement a larger emitter ring for a given magnet bore hole size. Considering the fundamental beam parameters, an excellent beam quality can be achieved in numerical simulations [41,42]. This inverse MIG is seen as major element for future high-power operation of multi-frequency gyrotrons particularly above 170 GHz.
- The wall-plug efficiency of a gyrotron determines the total efficiency of the EC heating system. Therefore, even if 50% total gyrotron efficiency is presently seen as sufficient for DEMO, the concept of a new multi-stage depressed collector (MDC) based on the $\mathbf{E} \times \mathbf{B}$ drift for the collection of the electron beam [43] has been advanced during the last EUROfusion research period. The two major advantages are a significant increase of the collector efficiency and at the same time, the possible reduction of the total power absorbed on the collector wall. In [44] it is shown that this concept could lead to collector efficiencies significantly above 70%, hence to total gyrotron efficiencies around 60%, considering a realistic electron beam - RF cavity interaction efficiency of 35%. In [45], the mechanical concept of a short-pulse MDC which considers compactness, manufacturability and as low as possible thermal wall loading is presented.

2.6. Operation at multiple possible frequencies and fast frequency step-tunability

The possible operation of a gyrotron operating at a set of frequencies that are multiples of the half- wavelength in the CVD diamond output window is becoming an important feature. Japan is known to have been the first to investigate this option for ITER [46,47]. It is a feature of Russian 105/140 GHz gyrotrons used in ASDEX Upgrade [48] and of the new French TH1510 84/126 GHz tubes used in TCV [49]. The latter are based on the TH1507 tube for W7-X.

Important for an efficient operation at multiple frequencies is a systematic cavity design approach that considers the caustic radii of the different operating modes very carefully. Since the begining of the EUROfusion program, the multi-frequency/multi-purpose operation has been an inherent part of the studies that were presented in [30] and [31]. A systematic design approach to select an optimal mode series for coaxial-cavity gyrotrons was presented in [50]. Considering the 170 GHz, 2 MW $TE_{34,19}$-mode short-pulse coaxial-cavity gyrotron pre-prototype at KIT the performance expectations have been theoretically investigated in [51] with very promising results. Based on that, a new modular-type 170/204 GHz coaxial-cavity gyrotron pre-prototype is under final preparation at KIT. In [52] and [53] the performance expectations and first results of the quasi-optical output coupler are discussed. The experimental verification of the quasi-optical output coupler at a very high order mode required the development of a novel automatic measurement system to verify its design at MW RF power level before inserting it in a gyrotron. The 170/204 GHz short-pulse pre-prototype will be tested in the new KIT 10 MW FULGOR gyrotron teststand including a new 10.5 T superconducting magnet [54].

For the TF Variant, frequency tunability in steps of 2-3 GHz in a range of ± 10 GHz around the main operating frequency is required to ensure the absorption of the radiation at the desired locations. The potential step-tunability of gyrotrons has been presented in [55] whereas its possible use in ITER and ASDEX Upgrade has been discussed in [56] and [57]. In [58] and [59] the step-tunable operation of a conventional hollow-cavity megawatt-class gyrotron with a high efficiency and a proper output beam Gaussian mode content was presented. A preliminary theoretical study on the possibility for stepwise frequency tuning of a dual-frequency 170/204 GHz $TE_{34,19}/TE_{40,23}$-mode coaxial-cavity gyrotron pre-prototype, under development at KIT, has been shown in [60]. A bandwidth of ± 10 GHz around both centre frequencies has been considered as tuning range. For each of the two bands, in total 11 modes have been selected to cover the entire frequency range. The theoretical study showed that the sole variation of the operating mode azimuthal index to obtain an appropriate mode series for frequency step-tunability is insufficient because the insert ohmic loading constraint is not fulfilled. A new mode series with reduced insert loading has been selected and will be investigated in near future experiments at KIT.

While the modular-type 170 GHz, 2 MW $TE_{34,19}$ coaxial cavity gyrotron is used for the verification of the fundamental capabilities of the coaxial-cavity technology, two questions may be raised: (i) what potential does the existing coaxial cavity offer with regards to MW-class multi-frequency operation also at two or three frequencies, such as lower and higher frequencies, and (ii) what could be a different mode selection to achieve an even higher output power in a more compact gyrotron design. Preliminary answers to these questions are provided in [61], in which the $TE_{25,22}$-mode was chosen and compared with the results obtained for the $TE_{34,19}$-mode. The extreme volume $TE_{25,22}$-mode allows to reduce the beam radius by around 25% and to increase the RF output power of the gyrotron by up to 30%. It shows that all the developed technologies are relevant and can be used to further raise the potential of a future coaxial-cavity gyrotron for DEMO.

2.7. CVD Diamond Brewster-angle window

The chemical vapor deposition (CVD) optical grade diamond RF Brewster-angle window concept has been one of the solutions under investigation for the option in DEMO of high power, continuous wave (CW) step-tunable gyrotron operation (TF variant). The window is shown in Fig. 12 with the diamond disk inclined at the Brewster-angle of 67.2°, which requires a minimum ⌀180 mm for the 63.5 mm waveguide aperture (compatible with an RF power of 2 MW-CW). In the PCD Phase of DEMO, the ambitious target of manufacturing a ⌀180 mm and 2 mm thick disk has been aimed for. That goal is well beyond the current technological limits of diamonds manufacturers and has been addressed by extensive dedicated diamond growth and polishing experiments by Diamond Materials[1] [62] in collaboration with loss tangent measurements at KIT. A successful and promising path has been developed, leading to some worldwide records as shown in Fig. 12 [63,64]. In parallel, the window design has been optimized and the cooling, thermal and structural performance of the window has been successfully characterized by dedicated numerical analyses, aiming also to investigate the sensitivity of the design [64]. Diamond growth and polishing experiments shall continue together with window prototyping and testing activities.

2.8. Future activities

During Horizon Europe, the EUROfusion Framework Programme 9 for Research and Innovation (FP9), the activities will mainly concentrate on the following key points:

- Evolution of the design from the pre-conceptual phase to the conceptual phase with focus on integration aspects that will necessitate interaction with other work packages such as Remote Maintenance and Handling (WPRM) and Breeding Blankets (WPBB).
- Continuation and refinement of the RAMI analyses to have a better estimate of the number of gyrotron and number of ports needed.
- Interaction with the Plasma System Division (PSD) to get an updated estimate of the power needs and their criticality.
- Selection of the gyrotron frequencies (136-170 GHz or 170-204 GHz or others).
- Demonstration of 2MW/1s pulse with a coaxial gyrotron.
- Development of a Brewster window.

3. ICRF antenna design for DEMO

Activities on the design of the Ion Cyclotron Range of Frequencies

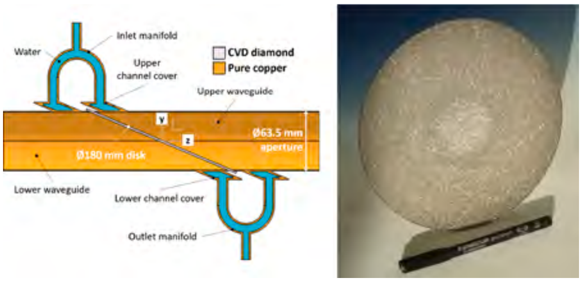

Fig. 12. Current window geometry (left) and worldwide first free-standing optical grade diamond disk with 180 mm diameter and average unpolished thickness of about 1.3 mm (right).

---

[1] The authors are thankful to Diamond Materials GmbH for the very fruitful collaboration.

antenna (ICRF antenna, operating at frequencies around 50 MHz for the DEMO parameters) within the framework of the EUROfusion WPHCD were recently concentrated on the development of a multi-strap antenna based on concepts similar to that of the ITER ICRF antenna and taking advantage of the ITER RoX. In the first place, it is aimed at providing means for ion heating using the ICRF system.

3.1. Progress in Antenna Optimization and Mounting Concept

3.1.1. Main Design Directions

The optimization process for the ITER-type ICRF antenna and of its mounting in DEMO involved three antenna development approaches based on the mounting procedure as shown in Fig. 13. As described in [65,66], the approaches shown in Fig. 13(b) and Fig. 13(c) aim at an increase of the antenna area relatively to the DEMO outboard port dimensions which limit the antenna size as in Fig. 13(a)

- Fig. 13(a) shows the so-called port-plug antenna with a small toroidal extent, fitting into the port without additional toroidal cut into the breeding zone. Such a solution might easily comply with the engineering constraints, and the mounting concept could be directly taken over from ITER. However, such an alternative will, for voltages imposed on the straps equal to cases (b) and (c), couple less RF power. For the above-mentioned port dimensions, an antenna with a maximum size of 1.04 m × 2.76 m (~2.9 m^2) is possible.
- Fig. 13(b) shows the antenna divided in two Poloidally Arranged Halves (PAH antenna) with an additional toroidal cut into the breeding zone of the BB shown in light green. The PAH approach could allow the largest possible area with fixed port dimensions. Assuming the port dimensions are limited to the maximum width of 1.08 m and the height of 2.8 m (the same as for the reference DEMO limiter port), the PAH antenna could reach dimensions of up to 2.16 m × 2.12 m (4.6 m^2). However, because of the large possible impact on the BB structures and a difficult installation procedure which would involve rotation of the antenna halves, this option was not pursued further. Therefore, the work concentrated on the two other development directions.
- Fig. 13(c) shows an antenna with an additional toroidal cut into the breeding zone of the BB with the Toroidally Arranged Halves (TAH). Assuming the maximum port dimensions mentioned above, this approach can use maximum antenna dimensions of 1.57 m × 2.76 m (~4.3 m^2). On the other hand, although the TAH antenna minimizes the impact on the BB compared to the PAH antenna, it has to be made compatible with the restrictions imposed for DEMO, like the maintainability and accessibility of the side components. It has also to be clear that this solution has a different mounting procedure compared to the ITER case where the antenna is a plug-in antenna fitting in the foreseen port. This mounting procedure is presented in Fig. 14, with graphs from the left to the right showing a top view of the mounting steps. One of the halves is inserted into the outboard port (step 1) and temporarily further inside and to the side of the port (step 2). The second half is then inserted (step 3) and mounted on its final position (step 4). At last, the first half is mounted on its final position and complementary components are mounted from the outside (step 5).

The coupled power depends significantly on the antenna design: (i) through possible voltage or current limitations in the straps and possible other components in the antenna system, and (ii) through the dominant $k_\parallel$ in the antenna spectrum. In general, smaller size antennas will require larger voltages for the same power capability, because of the higher inductance of narrower straps. Also, for the same relative phasing of the straps, a smaller inter-strap distance S_z between the strap columns will increase the dominant k_{z0} value, as follows from the relation $k_{z0} = \Delta\Phi/S_z$, with $\Delta\Phi$ the phase difference between two consecutive straps columns. This could also influence the power coupling.

3.1.2. Estimates for Coupled Power

In order to compare the power coupled by the two antenna options (a) and (c) described above, we consider in what follows three different antenna types as illustrated in Fig. 15: the ITER antenna as a reference (four strap columns, poloidal triplets), a DEMO antenna with the toroidal extent as the ITER antenna (four strap columns and poloidal quadruplets, 1.45 m x 2.7 m (~3.9 m^2)). This case is representative for a TAH antenna with quadruplets. We also consider for comparison a DEMO antenna with the same height as in the previous case, but scaled in toroidal direction to fit into the maximum DEMO port size of 1.08 m mentioned above, i.e. a DEMO port plug antenna with a surface of ~2.9 m^2. A large gap between the plasma and the antenna is anticipated in DEMO. On the other hand, a local gas puffing technique can be applied [67], in order to reduce the gap between the antenna and the fast wave cut-off, and thus increase or maintain the coupled ICRF power. For the calculations of the coupled power for the DEMO antenna options we assume the so-called "ITER2010low" plasma profile. This profile is considered as a pessimistic case for ITER and is representative of the DEMO plasma in the context of the application of a local gas injection technique.

The capability to couple power, as calculated by ANTITER II, for antenna types shown in Fig. 15, using the "ITER2010low" density profile, with 41 kV on the straps is shown in Fig. 16. Full triangles show the power coupled by a toroidally extended DEMO antenna (case II of Fig. 15). Full circles show the power coupled by the ITER antenna (case I of Fig. 15). For all phases shown we have:

$$J(k_\parallel)\,|_{k_\parallel=0} = 0 \tag{1}$$

but only for the phasing $[0,\pi,\pi,0]$ with same strap current amplitude or for the phasing $[0,\pi,0,\pi]$ with 1/3 current amplitude for both side strap columns both conditions

$$J(k_\parallel)\Big|_{k_\parallel=0} = 0 \text{ and } \frac{\partial J(k_\parallel)}{\partial k}\Big|_{k_\parallel=0} = 0 \tag{2}$$

are fulfilled, and correspond to the minimization of the antenna $E_\parallel$ field,

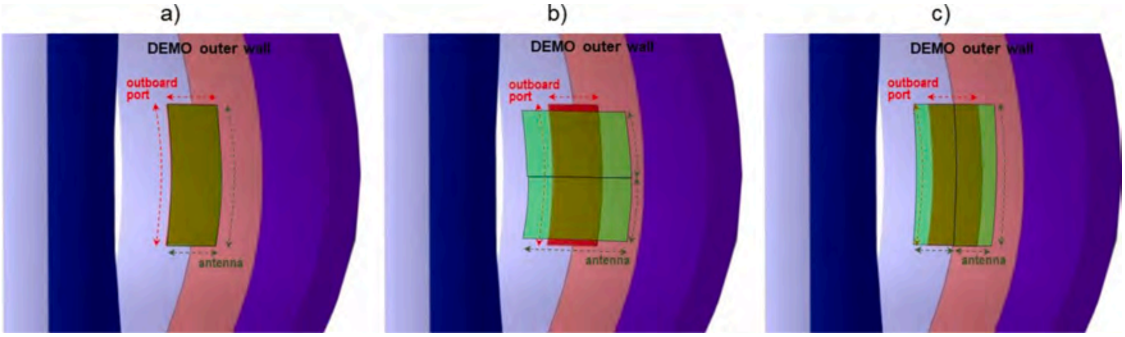

Fig. 13. Sketches of mounting for: a) port-plug antenna of the same width as the port size; b) PAH antenna; c) TAH antenna.

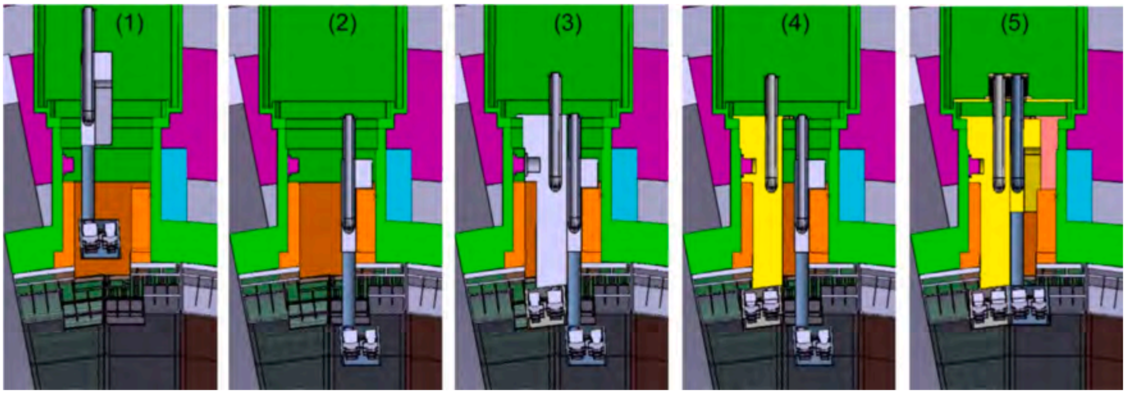

Fig. 14. From left to right: steps of TAH antenna mounting into the DEMO vessel, top view.

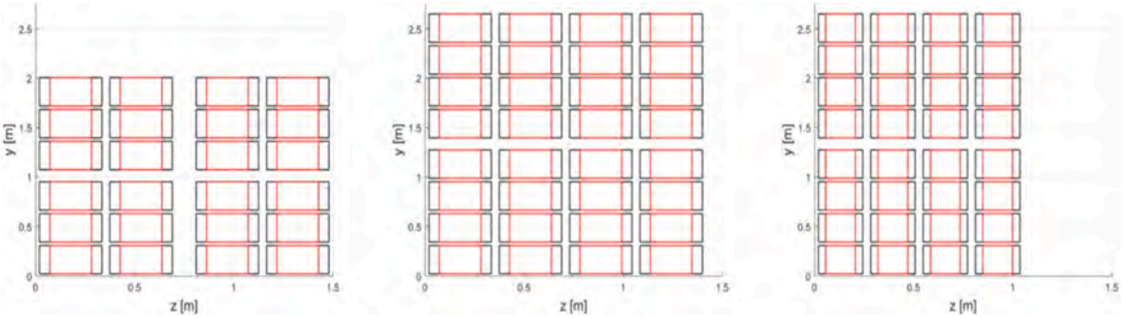

Fig. 15. Three antenna types used for coupled power comparison. Left (case I): the ITER antenna (four strap columns, poloidal triplets); Middle (case II): DEMO antenna with the same toroidal extent as the ITER antenna (four strap columns and poloidal quadruplets), representative for a TAH antenna with 3.9 m^2; Right (case III): a DEMO antenna with the same height as in the previous case but scaled in toroidal direction to fit into the DEMO port 1.08 m wide.

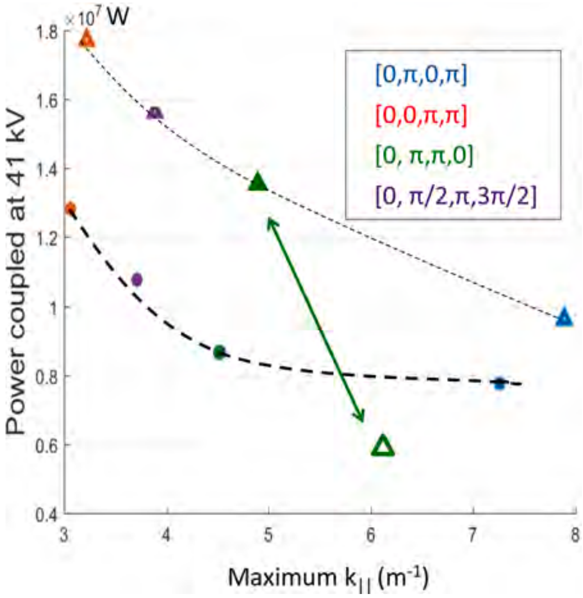

Fig. 16. Power coupled by a toroidally extended DEMO antenna. Circles: case I of Fig. 15 -ITER antenna, full triangles: case II of Fig. 15 - DEMO antenna, toroidally extended version, open triangle: case III of Fig. 15 - DEMO port plug, antenna for $[0, \pi, \pi, 0]$ phasing.

of the coaxial modes and of the associated edge fields, leading to the minimization of impurity production, as discussed below. These formulas express mathematically that the RF power transferred to surface waves and coaxial modes, corresponding to $k_{\|}$ values in the interval around $k_{\|} = 0$, should be minimized. A minimization procedure for the low $|k_{\|}|$ part of the antenna excitation spectrum can also be applied [68].

For the $[0, \pi, \pi, 0]$ phasing only, we added for comparison the power coupled by a DEMO port plug antenna (case III of Fig. 15). This is indicated by the open green triangle. One can clearly see that for the DEMO port plug antenna, the power coupled for the $[0, \pi, \pi, 0]$ phasing is substantially lower: from ~14 MW for the extended DEMO antenna, down to ~6 MW for the DEMO port-plug antenna. Therefore, for a possible port-plug solution, the port dimensions have to be increased at least to the dimensions of case II of Fig. 15.

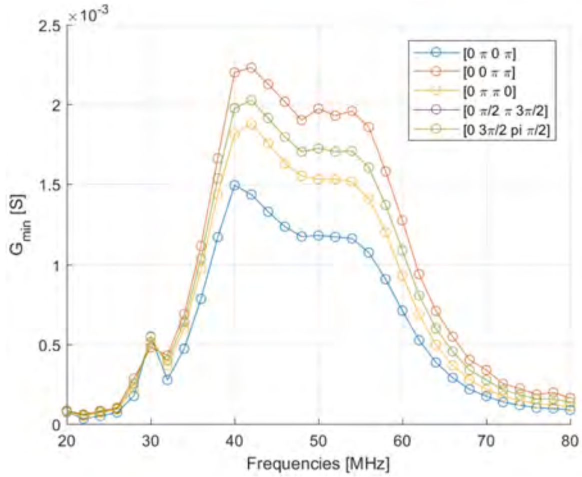

Fig. 17. Minimum conductance Gmin for the DEMO antenna case II of Fig. 15. Note that the green and purple lines for the current drive phasings ± [0, $\pi/2$, π, $3\pi/2$] coincide.

Fig. 17 shows the minimal conductance calculated by ANTITER II, for DEMO antenna case II of Fig. 15 as a function of the frequency, for different antenna phasings. The optimal $[0, \pi, \pi, 0]$ phasing performs better in terms of the coupled power (higher minimal conductance) than $[0,\pi,0,\pi]$. One can also see that such an antenna is capable of having the 15 MHz bandwidth as in ITER. A matching system similar as on ITER can be used on DEMO for this purpose [69]. This should be done considering the DEMO boundary conditions and in close collaboration with the DEMO design team. The optimization process is valid over the whole frequency range due to feedback control of the strap currents. Proof-of-principle tests on the ITER mock-up antenna have demonstrated that such an automatic feedback, containing 23 simultaneous actuators, can be very successfully implemented [70,71].

The calculations of the maximum coupled power with ANTITER II presented above in Fig. 16 agree well with the calculations by finite-element codes, such as HFSS, TOPICA and RAPLICASOL used for antenna simulations with a more precise antenna geometry. The cases with one half of the PAH antenna simulated using the finite element codes that include a plasma loading, TOPICA and RAPLICASOL were presented in [66].

Calculations for the more relevant TAH antenna were performed using HFSS, TOPICA and RAPLICASOL. The corresponding models based on the triplet strap configuration are shown in Fig. 18. The figure includes a) HFSS, b) TOPICA and c) RAPLICASOL models representing the reference planar TAH antenna with dimensions of 1.57 m × 2.76 m (~4.3 m^2). The HFSS model (Fig. 18(a)) shows the TAH antenna from the back, where the routing of the antenna feeders has been implemented using strip lines, in order to reduce the toroidal/poloidal space occupied by the transmission lines. The view of the TOPICA model (Fig. 18(b)) shows the antenna from the front with the mesh used in the code. The RAPLICASOL model (Fig. 18(c)) shows the antenna side view with the setup consisting of vacuum, plasma and PML (Perfectly Matched Layer), as well as with the radial RF electric field representing the fast wave propagation in the calculation domain.

The maximum transmission line voltages were calculated assuming a total power of ~50 MW with 3 antennas. This was done using the feeding parameters in the $[0, \pi, \pi, 0]$ phasing corresponding to the minimized local $E_{\|}$ at the antenna (as discussed below in Section 3.2.1) which also correlates to conditions (1) and (2). The voltages for the TAH antenna are 47.9-43.8-43.8-47.9 kV and 48.0-43.8-43.8-48.0 kV in TOPICA and RAPLICASOL respectively, with the same “ITER2010low” profiles as were used in the ANTITER II calculations presented in Fig. 16. It is important to note that a voltage of 45 kV in the transmission line corresponds approximately to 41 kV on the straps, the latter being the limit used for the power calculations above in Fig. 16. Taking into account that the case II antenna of Fig. 15 is ~0.4 m^2 smaller than the antenna in Fig. 18, both the ANTITER II and the finite element codes show that it is possible to couple about 50 MW from 3 antennas using an antenna with an area of about 4 m^2 and assuming the “ITER2010low” profile.

A curved CAD TAH antenna model was developed for the first Monte-Carlo N-Particle (MCNP) calculations. The calculations showed a good neutron screening behind the antenna. After further antenna design developments (see Section 3.1.3 below), the RF properties of this more realistic model will be assessed.

3.1.3. *Further Antenna Design*

Some of the options for the antenna with 3 toroidal straps were studied. However, for a 3-strap antenna that toroidally fits in the 1.08 m wide DEMO port, we do not have the same versatility as for a 4-strap antenna. A broader 3-strap antenna with the maximum possible area was studied with HFSS, but the transmission line voltages were further away from the optimum due to the smaller number of feeders than for the 4-strap options.

The TAH antenna presented in Figs. 18 and 19 used triplets as strap solutions. The benefit of using short strap triplets/quadruplets fed in parallel with respect to one long strap is apparent in Fig. 20. For triplets/quadruplets fed by 4 or 5 port junctions with voltage antinode at the junction point we find a much more constant current, a lower maximum voltage, and a larger radiated power, as clearly illustrated in Fig. 20 below. The larger poloidal extent of DEMO imposes to reassess the segmentation in triplets that was used for ITER. For a TAH geometry configuration, the segmentation into quadruplets was shown to be the optimum case, minimizing both the maximum parallel electric field at the strap feeder $E_{\max}$ and the maximum voltage on the transmission line $V_{\max}$ of the matching system [72]. Fig. 20(c) presents the maximum $E_{\max}$ and $V_{\max}$ estimated with ANTITER II to couple 17 MW with a TAH antenna geometry as a function of the number n of segments of a strap. As it is optimal, the quadruplet design was used in the ANTITER II calculations presented below. The study of the practical implementation of

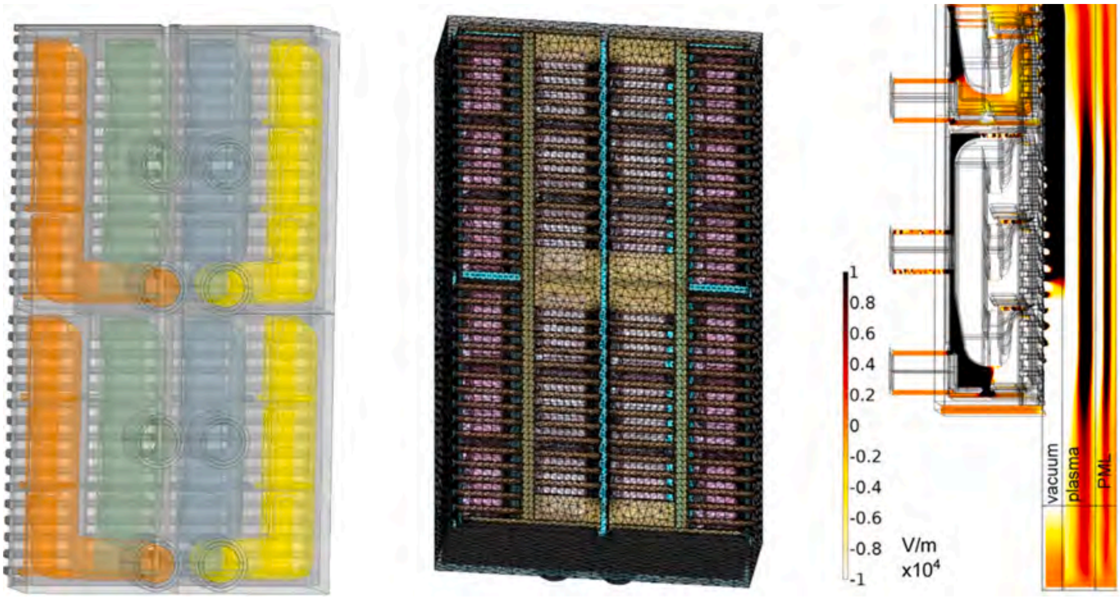

Fig. 18. Models for simulations of the reference TAH antenna: a) back view of the HFSS model with rerouting of the feeders visible; b) front view of the TOPICA model; c) side view of the RAPLICASOL model with radial RF electrical field representing fast wave.

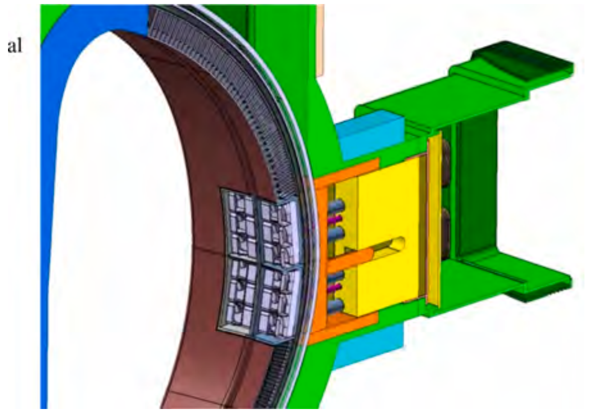

Fig. 19. TAH antenna CAD model integrated in DEMO.

quadruplets in the antennas using the finite-element codes is planned.

It is foreseen to explore several other options for the antenna developments, such as using a larger antenna depth in the region of the central straps for the TAH antenna, implementing the curvature of the antenna surfaces to fit the banana shape of the BB (effectively developing the model from Fig. 18), or tilting toroidally the antenna elements. The effect of the poloidal phasing should also be further studied with the finite-element codes.

Thus, the most promising concepts are being identified and developed further, but it is still too early to select a single solution with specific characteristics. In addition, a number of uncertainties still remain, such as the arrangement of the BB and the exact size of the DEMO ports. Finally, it is important to point out that the ICRF antenna optimization in ITER is still ongoing. It is expected that this will result in further insights, useful for the ICRF design options on DEMO.

3.2. *Optimization: Minimization of Local $E_{\|}$ and of Coaxial modes*

Two optimization approaches are used during the antenna development. Approach (I) is minimizing the local $E_{\|}$ at antenna Plasma Facing Components (PFCs) which for the DEMO geometry means antenna sides. The other Approach (II) aims at minimizing the excitation of coaxial and surface modes at the plasma edge. The approaches are complementing each other rather nicely, but the full physics link between the two approaches is a subject of active research. To start, we summarize the main aspects of both approaches one by one (Sections 3.2.1 and 3.2.2), and then discuss the relations between them (Section 3.2.3).

3.2.1. *Approach (I): Optimization of the Local $E_{\|}$ Close to Antenna PFCs*

The direct local $E_{\|}$ excitation by the RF current-conducting antenna PFCs (in particular, antenna sides) can drive the RF sheath effects directly at the antenna. The local $E_{\|}$ can be excited electrostatically (mostly by voltage between straps and the antenna sides) or electromagnetically coupled to the plasma (mostly parallel RF image current $j_{\|}$ on conductive antenna elements, in particular antenna sides). By acting on both excitation mechanisms, the local $E_{\|}$ can be minimized by adjusting the antenna geometry, e.g. by field-aligned Faraday screen, by non-protruding (out of the wall) antenna parts (as for the broad-limiter antenna) or by the field-aligned antenna. At the same time, the local $E_{\|}$ can be minimized by reducing the local $j_{\|}$ by antenna feeding, in particular by selecting a proper power balance in the dipole phasing.

The modification of the local $E_{\|}$ effects using the power balance was first experimentally shown on the 2-strap antennas on Tore-Supra (TS) [73]. The ICRF-specific heat loads on the antenna plasma facing components showed an increase close to the strap coupling more power, and a decrease close to the strap coupling less power, when changing the power balance from 50%/50% to 63%/37% in the dipole phasing. Then it was shown on ASDEX Upgrade (AUG) [74] that the toroidal RF current (which equals approximately $j_{\|}$) measured at the antenna sides (and the correlating W source in other locations - see details in [74]) experiences a minimum as a function of voltage balance between the straps. The above-mentioned local quantities can be reduced significantly when the power balance is changed. For the 2-strap antennas, the reduction works only for one antenna side at once, while the other side experiences an increase. This behaviour was successfully described by the local $E_{\|}$ values (a consequence of local $j_{\|}$) calculated by HFSS and TOPICA.

A case in which a reduction of $E_{\|}$ on both antenna sides at various locations regions and at a similar (but not exactly identical) antenna feeding can be obtained, is that of the 3-strap antenna, also in use on AUG [75]. The reduction of $E_{\|}$ allowed to decrease the local W source at the antenna which was dominant for the 2-strap antennas. The poloidal asymmetry in the minimization of the local RF fields and local W sources was observed in the experiment [75]. As is shown in [75], the behaviour could be well described by the local value of $E_{\|}$ (averaged over the limiter tiles) from the TOPICA calculations which showed very similar location-dependent characteristics as the experiment. It is important to note that the optimum power balance and phasing is varying significantly from location to location (both toroidally and poloidally), both in the experiment and the calculations.

In the AUG experimental conditions, where the slow wave is usually strongly evanescent at the plasma facing components (antenna limiters), the local $E_{\|}$ at the antenna limiters was found as the most relevant physics parameter to describe the behaviour of the local W source.

General minimization of $E_{\|}$ is pursued during the development of the ITER-type ICRF antenna for DEMO. Fig. 21 shows $E_{\|}$ for the TAH antenna, as calculated using HFSS and the model from Fig. 18(a) [66], as a function of the feeding parameters. The figure shows the $E_{\|}$ values averaged over the areas which are closest to the plasma facing

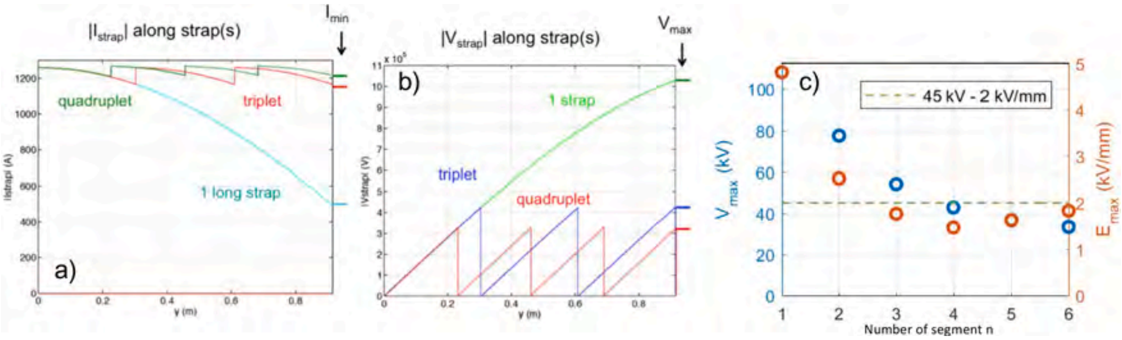

Fig. 20. Effect of using a single strap, triplets or quadruplets and on current a) and voltage b) along the strap; c): maximum voltage $V_{\max}$ and electric field $E_{\max}$ on the matching lines for a segmentation n of long straps and 17 MW coupled by the antenna using TAH configuration operating at a maximum voltage of 45 kV or an equivalent electric field of 2 kV/mm in the toroidal direction.

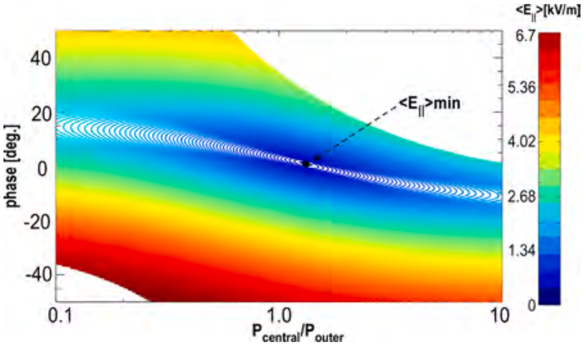

Fig. 21. Minimization of $E_\parallel$ for the TAH antenna [66].

components. The field experiences a clear minimum corresponding to the projected working point. The full optimization involves a minimization of the maximum values and the avoidance of local peaks of $E_\parallel$.

3.2.2. Approach (II): Minimization of the Edge Modes

$E_\parallel$ can also be excited indirectly via a wave transformation, namely by the wave confluence between the fast and slow wave that occurs in the scrape-off layer (SOL) for non-inverted heating scenarios, as is shown by the approach describing the excitation of the coaxial and surface modes.

To this end, the semi-analytic code ANTITER IV, an extension of ANTITER II, was developed. ANTITER IV solves the set of equations that result from the cold dielectric plasma tensor in an inhomogeneous plasma and Maxwell's equations in plane geometry with a Fourier analysis in the direction of the total magnetic field z and the y direction which is perpendicular to the z (defined above) and radial x-directions. This analysis takes into account the toroidal and poloidal periodicity of the fusion device, by the choice of the eigenvalues of k_z and k_y.

The difference is that in ANTITER II the equations are considered in the zero electron-mass limit, which reduce then to a set of two first order differential equations. The code thus describes only the fast wave, and the confluence between the fast and slow wave is approximated by the Alfvén resonance as illustrated in Fig. 22.

The slow wave has a singularity (i.e. a higher order confluence with an Ion Bernstein wave) at the LH (Lower Hybrid) density. In order to work around the singularity, in the ANTITER IV model a small amount of collisions is considered in the cold plasma tensor terms, as in [76]. In the absence of collisions, several wave components are infinite at the singularity. The precise description of the damping is not easy as it requires a kinetic approach to consider the conversion to an ion Bernstein wave and also non-linear effects due to the high fields. A discussion of these effects is given in [77].

Fig. 23 gives an example of the output of the code, with the presence of coaxial modes and surface modes along the Lower Hybrid density.

At or below the LH resonance density, surface modes can be excited that propagate far from the antenna location (see [78]). The tentative explanation of the decay of the surface wave along z with ANTITER IV is that this surface wave consists of a packet of slow wave components corresponding to k_{zn} and k_{ym} eigenmodes with different phases (because their confluence with the fast wave is k_z dependent) and that the decay is due to the loss of coherence between the different waves in the packet.

To remedy this excitation, one must exclude to excite $k_\parallel$ values in the region $|k_\parallel| \leq k_0$, where k_0 is the vacuum propagation constant. This translates into the two conditions (1) and (2) described in Section 3.1.2 above (see [78] for more details). In [78], a correlation is shown between the conditions needed to avoid exciting the $|k_\parallel| \leq k_0$ region and the minimization of the radial electric field amplitude. Ref. [78], as well as Section 3.2.3 below study also the correlation between the exclusion of surface and coaxial modes and minimizing impurity release.

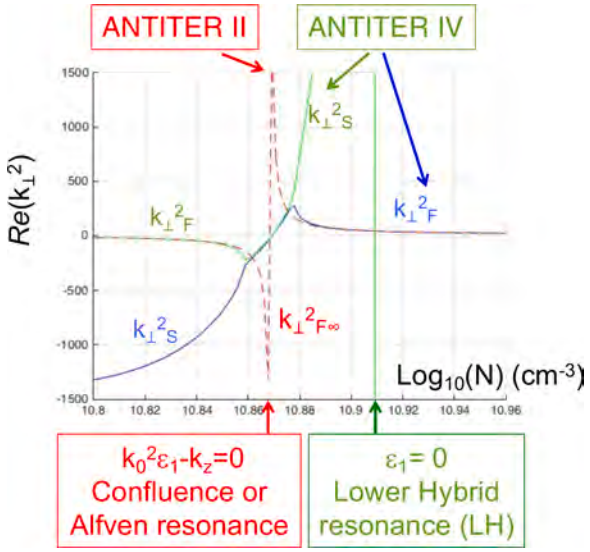

Fig. 22. Example of the dispersion relation as a function of the plasma density as calculated by ANTITER II and ANTITER VI. The red-dashed line is the simplified dispersion relation of the fast wave in the limit of zero electron mass, used in ANTITER II. The confluence between the slow and fast wave is in that case represented by the Alfvén resonance. The green and blue curves result from the 4th degree dispersion relation for the fast and slow wave as used in ANTITER IV. The strong link between the slow and fast wave in the confluence region is now clearly seen. The asymptote of $k^2_{\perp,s}$ is in this case given by the Lower Hybrid resonance, which is the correct solution for the cold plasma case.

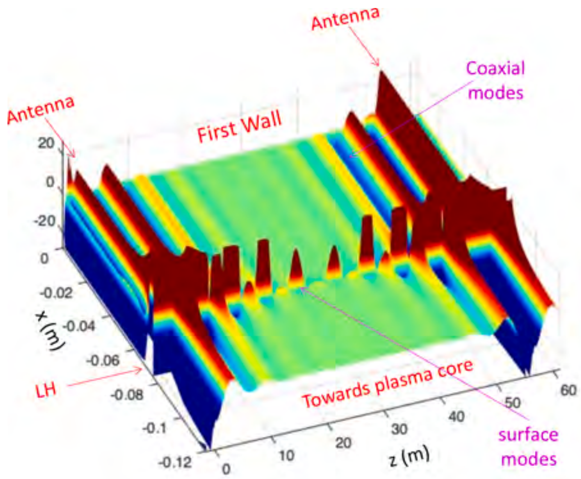

Fig. 23. Typical output from ANTITER IV. The torus is unfolded at the antenna position. The antenna launches RF power at x=0 cm. Surface waves and coaxial modes are clearly seen. The coaxial modes are located between the location of the LH resonance and the edge. Surface waves appear at the density corresponding to the Lower Hybrid density in the edge.

3.2.3. Relation between the Two Approaches

In the case of a 2-strap antenna with imbalanced strap powers, there is no correlation between the conditions for the local decrease of $E_\parallel$ on one antenna side and the conditions for the $k_\parallel$ spectrum contribution at $|k_\parallel| \leq k_0$. Fig. 24 shows the modification of the $k_\parallel$ spectrum of the AUG 2-strap antenna when changing the voltage balance as in the experiment from [74]. The change of the voltage balance as in the experiment for the TS antenna from [73] would produce a similar $k_\parallel$ spectrum modification. The antenna-averaged temperature on the antenna PFCs (TS), as well as the RF current on the limiters (AUG, same applies for W source) do not change significantly during these power balance scans. Thus, the

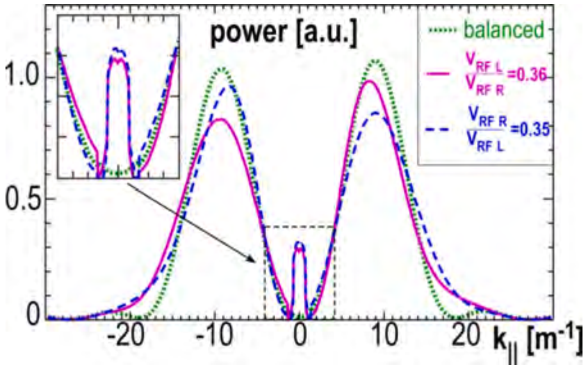

Fig. 24. $k_{\parallel}$ spectrum of the ASDEX Upgrade 2-strap antenna, with balanced strap voltages (dotted green line) and unbalanced strap voltages (solid magenta and dashed blue lines).

strong increase of the power at $|k_{\parallel}| \leq k_0$ in Fig. 24 does not correlate with the antenna-averaged temperature on the TS antenna, neither with the antenna-averaged RF current and/or W source on the AUG antenna. Therefore, in the case of a 2-strap antenna and the strong toroidal asymmetries of the antenna feeding, the results of approaches (I) and (II) can deviate significantly from each other.

Nevertheless, for the more reactor-relevant cases of the toroidally symmetrical feeding of the 3-strap antenna with $[0, \pi, 0]$ phasing, and of the 4-strap antenna with $[0, \pi, \pi, 0]$ phasing, the two approaches lead to similar conclusions, at least when minimizing $E_{\parallel}$ averaged over the full poloidal and toroidal extent of the antenna. This is related to the fact that both antenna-averaged $E_{\parallel}$ and power in the $|k_{\parallel}| \leq k_0$ spectral domain can be efficiently excited by the imbalance of the antenna strap currents with toroidally (quasi-) symmetric antenna feeding laws. On the one hand, the different physics related to approaches (I) and to (II) can overlap in the toroidally (quasi-) symmetric cases: in (I) the slow wave is launched directly by the antenna; in (II) the slow wave appears mostly due to the wave transformation from the fast wave to the slow wave. On the other hand, following both approaches and ensuring the minimization of both effects at the same time provides a better confidence in the success of a new antenna. This is especially important, because for the future machines like DEMO the slow wave propagation region can extend over a larger region of the scrape-off layer. In the experimental conditions of most of the current machines, the slow wave is usually propagative only deep in the main limiter shadow.

For the particular $[0, \pi, 0]$ and $[0, \pi, \pi, 0]$ cases with toroidally symmetric feeding, one can use the correlation of the conditions in practice, by applying the analysis of the coaxial part of the power spectrum, i.e. $k_{\parallel}$ spectrum contribution at $|k_{\parallel}| \leq k_0$ and using it also as an approximate representative of the averaged $E_{\parallel}$-field excited by the antenna directly. Conditions (1) and (2) for the strap currents from Section 3.1.2 can thus be used for minimizing the impurity release. Consequent checks of the local $E_{\parallel}$ field and its distribution can also be made, if details are required.

One of the first results obtained with the 3-strap antenna in AUG [79] was the minimum-like behaviour of the measured increment of the core W along with the increment of the antenna-averaged W sputtering as a function of the ratio of the RF power on the central strap to the sum of the power in the 2 outer straps, $P_{\text{central}}/P_{\text{outer}}$ and operating the antenna with the $[0, \pi, 0]$ phasing. These measurements effectively represent antenna-averaged quantities of the locally measured W sources from [75]. When comparing this to Fig. 25, presenting the fraction of the radiated power into the coaxial part of the power spectrum (at $|k_{\parallel}| \leq k_0$) in % versus $P_{\text{central}}/P_{\text{outer}}$, the similarity of the theoretical curve with the experimental values is striking, with a minimum for the power ratio $P_{\text{central}}/P_{\text{outer}}$ and a very similar asymmetry around this minimum.

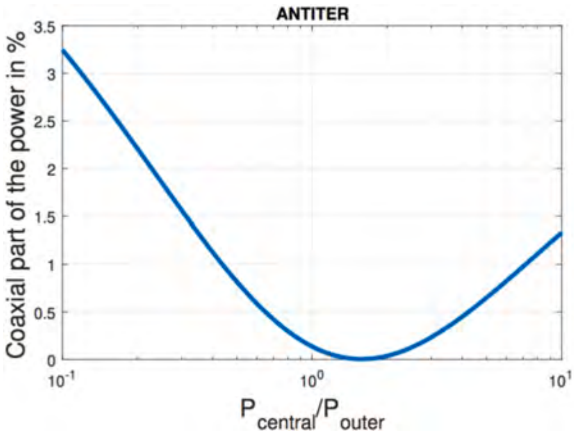

Fig. 25. Coaxial fraction of the launched RF power versus $P_{\text{central}}/P_{\text{outer}}$ calculated for AUG.

The AUG method to reduce the impurity release by the ICRH antenna was also successfully applied on Alcator C-Mod using the field-aligned antenna with $[0, \pi, \pi, 0]$ phasing and varying the powers fed into the two inner (P_{central}) and outer straps [80] with total power P_{total}. The coaxial part of the power spectrum computed using ANTITER II is plotted in Fig. 26 as a function of $P_{\text{central}}/P_{\text{outer}}$. Comparing the figure to the experimental results for the impurity concentration [80], they are again similar, with an asymmetric curve around a minimum value for $P_{\text{central}}/P_{\text{outer}}$. The minor difference in the position of the minimum measured in the Alcator C-Mod experiment and our calculated results may be due to the difference between the simplified model and the real geometry of the Alcator C-Mod antenna with its folded straps and field alignment.

To summarize, using both approach (I) to minimize the local $E_{\parallel}$ and approach (II) to minimize the excitation of the coaxial and surface modes by minimization of the power in the $|k_{\parallel}| \leq k_0$ domain combines the strengths of the tools used for the antenna design. As a consequence, the performed analyses can be cross-checked and provide further insights in the physics involved. Finite-element codes such as HFSS and TOPICA describe the near-field patterns using an accurate antenna geometry based on the minimization approach validated experimentally in AUG. The model in ANTITER II describes the wave transformation from the fast wave to the slow wave which could play a more important role for the future machines. In the novel code ANTITER IV, which uses simplified antenna geometry, but full density profile, the direct excitation of the slow wave can now also be taken into account, including the interaction of the slow and fast waves from the antenna location up the

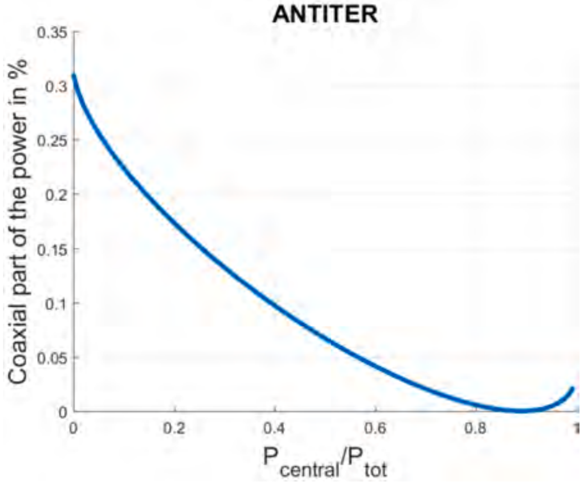

Fig. 26. Coaxial fraction of the launched RF power versus $P_{\text{cent}}/P_{\text{total}}$ calculated for Alcator C-Mod.

location of the LH density. More recent developments of the COMSOL-based RAPLICASOL code also allow for the full-wave description, including the precise description of the slow wave behaviour [81].

3.2.4. The Amount of the RF power Lost in the Edge

The power lost in coaxial and surface modes has been evaluated for the different toroidal phasing cases on the example of the ITER antenna and the much better performances of the $[0, \pi, \pi, 0]$ phasing with equal current amplitude in each strap is striking: only 0.6% of the power is lost in edge wave propagation. The total power spectra calculated by both ANTITER II and the new code ANTITER IV for the ITER antenna, including the effect of the poloidal magnetic field, are shown in Fig. 27 (left). There is overall a good agreement between the results of both codes when the Faraday screen of the antenna is field aligned, as can be seen from the close proximity of the two curves presented for each phasing. Fig. 27(right) shows a zoom in the low $k_{\|}$ region, as calculated by ANTITER IV. This figure shows very clearly that in the case of the $[0, \pi, \pi, 0]$ phasing the radiated power in the low $k_{\|}$ zone, responsible for edge power loss, is much lower than for the other phasings. This is also confirmed in Fig. 28(left), showing the $k_{\|}$ spectrum of the edge power losses only, obtained from the difference of the total Poynting's flux at the antenna aperture and the flux towards the antenna centre for densities larger than the LH density. This edge power losses spectrum due to the slow wave excitation is limited to the region $|k_{\|}| \leq k_0$, because the slow waves responsible of the edge losses are only excited by confluence with the fast wave for $|k_{\|}| \leq k_0$.

Let us consider the case when the Faraday screen is not field aligned. A direct E_z excitation of the slow waves is possible that extends above $|k_{\|}| = k_0$ [82]. An example is shown in Fig. 28(right) for the Faraday screen aligned with the antenna and both having a tilting angle of 15° with respect to the total magnetic field. The power loss is larger with not field aligned screen but it can also be mitigated by the depletion of low $|k_z|$ excitation, and also by increasing the density gradient in the region of LH resonance.

An optimized gas puff is able not only to produce a significant increase of coupling, but also to decrease the ratio of edge power loss to the power coupled to the core plasma by acting on the plasma density profile in front of the antenna [67].

The main power loss mechanism for $E_{\|}$ at the antenna is RF sheath losses. These can be estimated using the combination of the RAPLICASOL and SSWICH-SW codes which were successfully used to describe the experimental data from TS, AUG and JET. It is not expected that considerable losses for the optimized conditions will appear, but the calculations are planned for the future.

3.3. Ion Heating with Optimized Antennas

For the cases considered here, the effect of the launched $k_{\|}$ on partitioning between heating ions or heating electrons is relatively small. The partitioning depends mostly on the heating scenario, on the absorbing particle and on the kinetic plasma profiles.

There are several options to heat the ions using ICRF in D-T plasmas all of which work in the whole range of the $k_{\|}$ values of 4.5-6.2 m^{-1} for which the minimized $E_{\|}$ and edge losses are possible (see Section 3.2):

i Second harmonic heating of tritium ions, assisted by fundamental cyclotron heating of ^{3}He (a few percent), is considered for D-T plasmas in ITER to maximize bulk ion heating and increase T_i, especially during the ramp-up phase of the plasma pulse to bring the plasma to the required fusion-relevant temperatures. This scenario has been studied experimentally on TFTR and JET, and has shown good performance [83]. E.g. at TFTR, applying an additional amount of only 5.5 MW of ICRF at the second harmonic of tritium in D-T supershots on top of 23.5 MW of NBI resulted in an increase of the central ion temperature from 26 to 36 keV [84,85]. For this heating scenario in DEMO, the dependence on the toroidal mode number between $n_{\|} = 53$ and $n_{\|} = 73$ (corresponding to the $k_{\|}$ range above) is presented in [86]. Although the lower $n_{\|}$ values are favoured for ion heating, which at high T_e and n_e competes with direct electron heating, the dependence in this range on the toroidal mode numbers is quite weak and any $n_{\|}$ value in the range would provide ion heating.

ii Recent heating experiments using the novel 3-ion scenario [87–89], confirm its high efficiency to deposit RF power to ions. Moreover, 3-ion scenarios are very flexible and not limited to using H, D or He isotopes as resonant absorbers. Heavier ions can be used as well, as observed years ago (but the importance was not realized as such for use in later experiments) in earlier D-T experiments on TFTR and JET.
  - During wall conditioning in supershots (discharges with high performance) in TFTR using natural Li pellets, ^{7}Li ions were identified as absorbing the bulk of the RF power. In fact, the 3-ion T-(^{7}Li)-D ICRF scenario was effectively at work.
  - Similarly, in D-T plasmas in JET with the C-wall, rather unexpectedly strong absorption on ^{9}Be ions heating was identified [83]. The amount of ^{9}Be present was ~1%. In fact, the T-(^{7}Li)-D scenario was at work, as hypothesized by the authors, but now fully confirmed reconsidering the data of these discharges. Numerical simulations for this T-(^{7}Li)-D show also that for a fairly broad range for the D-T isotopic ratio in the plasma, including D: T=50%-50%, RF power absorption should be very efficient at ^{9}Be concentrations in the range of 1%. Note also that this ^{9}Be ICRF heating scenario is moreover compatible with additional seeding of Ar and ^{22}Ne impurities (candidate ions for impurity seeding), having a very similar charge-to-mass ratio as ^{7}Li.

It is important to underline that as a result of their larger atomic mass, heavier impurities transfer an even larger fraction of absorbed RF power to bulk D and T ions than He or H isotopes, as follows from basic Coulomb collision theory. Accelerating heavy impurities is a natural extension of the application of 3-ion scenarios, and much more difficult

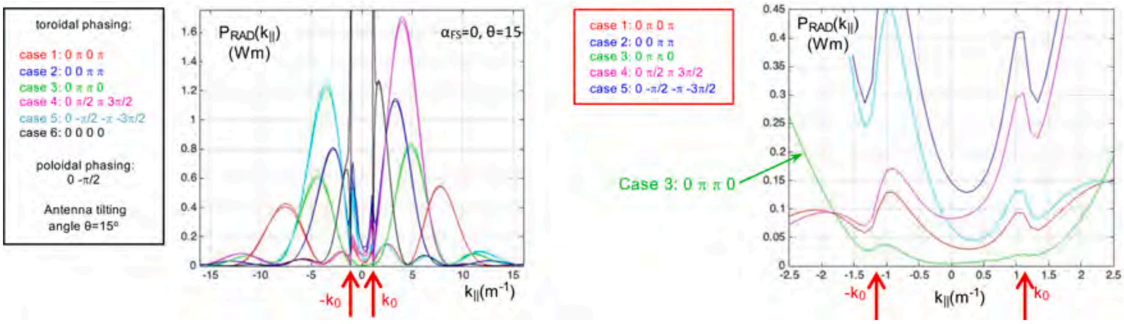

Fig. 27. (left) Total ITER antenna power spectra from ANTITER II & IV; (right) Zoom in the low $k_{\|}$ region.

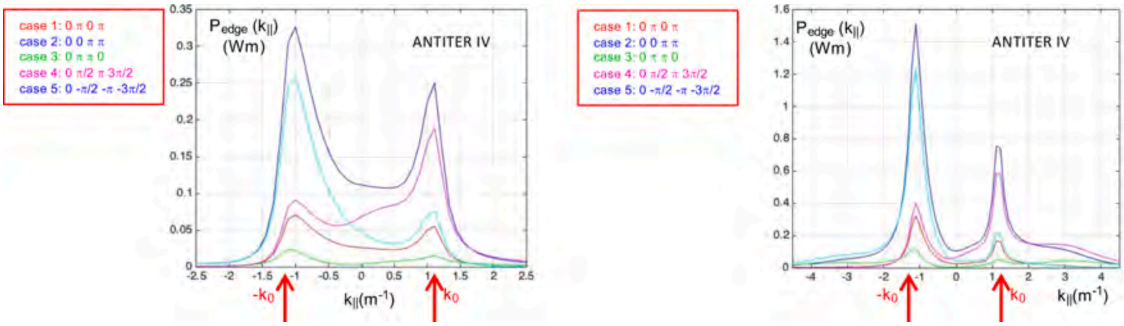

Fig. 28. (left) Power spectrum (for 1A in every strap) of the edge power deposition from ANTITER IV with field aligned screen and antenna tilted by $\theta = 15^\circ$. (right) Power spectrum (for 1A in every strap) of the edge power deposition from ANTITER IV with field not aligned screen ($\alpha_{FS} = 15^\circ$) and antenna tilted by $\theta = 15^\circ$.

to reach with other heating systems. The 3-ion scenarios are therefore ideally suited to realise an optimal transfer of launched RF power to the plasma ions by direct RF absorption but also during the slowing down of the heated particles with a proper choice of the absorbing ion.

Table 2 shows the power split between electrons and D^+ and T^+ ions for the D-T-(^{3}He) at the fundamental frequency of ^{3}He and the T-(^{9}Be)-D 3-ion heating scenario at the fundamental frequency for ^{9}Be. Power distributions among the species before (direct heating) and after the collisional transfer (collisional heating) are shown. There is a slight difference in 10 MW and 20 MW heating as the absorbing particles becomes more energetic in the last case, and thus deposits slightly more to the electrons.

The requirements for $k_{\|}$ for good coupling with the scenarios mentioned are the same as for other ICRF scenarios.

In addition to the ion heating, it needs to be noted that ICRF power is becoming a powerful tool to stabilize the core turbulence by tailoring the fast ion population. Several mechanisms have been studied so far (see e.g. [90,91]) with more results anticipated in the near future [92]. The effectiveness of those mechanisms in presence of a large alpha particle population, like expected in DEMO, needs however further analysis.

4. Neutral Beam Heating System

For pulsed DEMO operation, a high energy Neutral Beam Injector (NBI) can contribute during the various plasma phases [93]. NBI can indeed provide core power during the current-ramp phase above a certain plasma density, easing the so-called “heat-to-burn” and L-H transition through considerable ion heating during ramp-up and balancing radiation losses during ramp-down [94]. Although current-drive is not a specific requirement for pulsed DEMO, high energy NBI is also capable to drive a significant plasma current, which can help in saving central solenoid flux and in extending discharge duration. In the flat-top phase NBI can contribute to the burn control of the plasma. While the heating mix of DEMO [95] is foreseen to be considered in 2024, the current functional requirement for the NBI system of DEMO is to provide 50 MW of core plasma heating by means of deuterium neutrals (D^0). Three NBIs delivering about 17 MW each are foreseen.

Table 2
Overview of the transfer of the launched RF power to the different plasma species. The significant influence of the mass of the absorbing ion on the final transfer of RF power to the plasma ions is illustrated by comparing ^{3}He and ^{9}Be as absorbers for 10 and 20 MW launched RF power as will be required in ITER.

RF power split	Electrons (%)	Absorbing minority (%)	D and T ions (%)
D-T-(^{3}He)–50%-50% D-T with a small amount of ^{3}He			
Direct heating	9	76	14
Collisional heating (10 MW)	29	5	62
Collisional heating (20 MW)	43	5	50
T-(^{9}Be)-D–50%-50% D-T with a small amount of ^{9}Be			
Direct heating	6	76	12
Collisional heating (10 MW)	10	5	81
Collisional heating (20 MW)	17	4	76

The design has been developed based on the ITER NBI, from which an important RoX is expected. The key components of the design are similar to the ITER design: negative ion sources at high voltage, negative ions production using Cs, beam energy of 1 MeV, similar power per injector. However, some DEMO requirements are different: one of them is related to the pulse duration (7200 s for DEMO, compared to 3600 s for ITER [96]) leading to the need for an improved Cs management system. While the reference neutraliser is a gas one, a beam driven plasma neutraliser (BDPN) is considered as part of the R&D activities.

The design of DEMO NBI takes into account the return of experience from the existing negative ion-based neutral beam injectors (JT60 NBIs, LHD NBIs), the existing test facilities on negative ions for fusion (ELISE, BATMAN and SPIDER in Europe, MTF and NITS teststands at QST Japan, RNIS teststand at NIFS Japan), and from the neutral beam injectors under design or construction (MITICA, ITER DNB, ITER HNB, DTT NBI)

The section will first describe the conceptual design phase and R&D activities, followed by physics studies for specific NBI sub-systems.

4.1. *Concept Design - Engineering Activities*

4.1.1. *Background*

Following NBI-plasma interaction studies [93], an optimized injection of high energy beams of deuterium neutrals (D^0) should be, for a pulsed DEMO, tangentially directed in the plasma, co-current, and aimed at the plasma core. In order to lower possible shine-through fast particle losses during low-density phases, beam trajectory should avoid any intersection with the inner wall. Tilting of the beam line does not provide any clear advantage. 1 MeV energy has been shown to be in the optimal range for plasma requirements, with a NBI operational window even larger than ITER case at low densities.

4.1.2. *Design Description*

Other fundamental choices driving the design [97], are an average divergence of the beamlets lower than or equal to 7 mrad, a target beam-on time of 7200 s, a co-extracted electron fraction (e^-/D^-) lower than 1 and a power per beam line of about 17 MW.

Compared to the previous version of the DEMO NBI [97], the most updated design described here allows to exploit the return of experience from the existing experiments, in particular the ones related to the ITER HNB, i.e. the NBTF [98] and ELISE [99]. Other positive points will be described in the following, such as the outcome of the RAMI analysis carried out on the beam source and the developments on key aspects like the beam optics, the RF drivers, the caesium management, the pumping systems and the neutralization process.

The 2021 concept design of the DEMO NBI, shown in Fig. 29, features the same beam energy (1 MeV) and the same number of accelerator grids (7) as in ITER HNB, separated by an extraction gap of about 10 kV (distance between the grids of 6 mm) and 5 acceleration gaps of 200 kV each (with a distance between the grids of 105 mm). The geometry and number (1280) of the apertures for the beam extraction, as well as the design of the accelerator support frames (with a 'bathtub' shape) and related insulators are also similar to ITER HNB. Other points in common with the ITER HNB are the Beam Line Components (BLCs), i.e. the neutralizer, residual ion dump and calorimeter, the transmission line insulated in SF_6 and the fast shutter and absolute valve at the exit of the beamline. Regarding the BLCs, the Beam Driven Plasma Neutralizer [100] could be an alternative option to the reference Gas Neutralizer (GN) if the on-going studies will prove the concept.

The main differences from ITER HNB ar as follows :

- There is no tilting mechanism, but instead the beam source is rigidly connected to the beam source vessel. In fact, the tilting of the beam source implies significant complications to the design and is not required for DEMO.
- Each grid is composed of 8 square-like segments with dimensions of about 0.5 m × 0.5 m, fixed to a stainless steel frame, to obtain a better alignment and an easier manufacturing of the copper parts. For a proper beam aiming, each segment has a vertical bend and is supported by means of fixed and sliding pins designed to minimize the possible misalignments between the corresponding apertures of different grids due to the thermal deformations foreseen during operations.
- Two ion source modules are foreseen having dimensions of about 1 m × 1 m (similar to ELISE [99]), each featuring 2 racetrack RF drivers as described in [101].

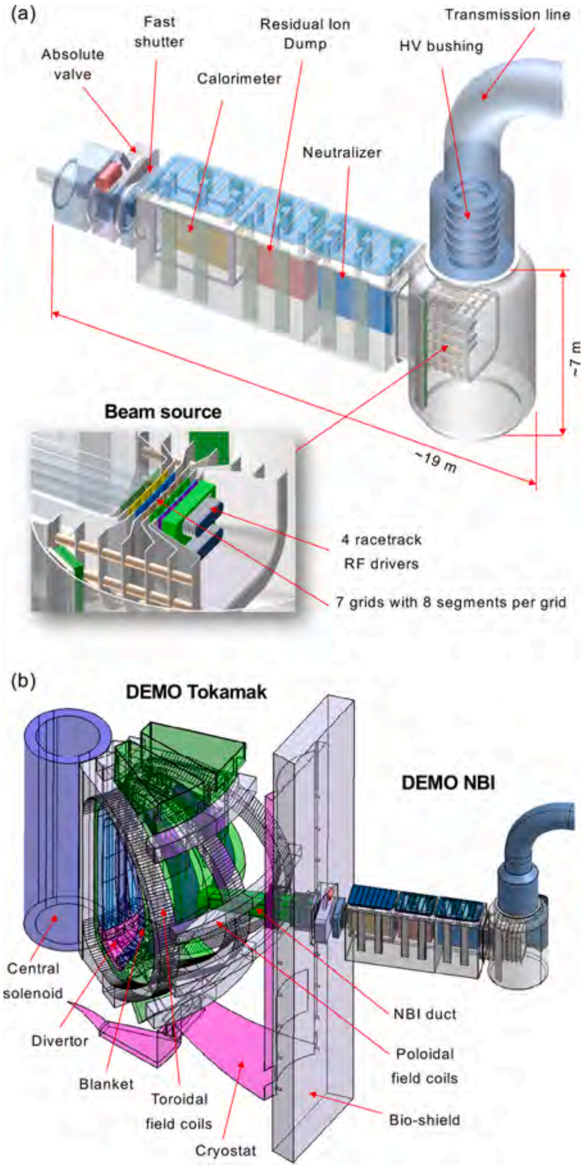

Fig. 29. DEMO NBI 2021 concept design: (a) overall view with focus on the beam source; (b) integration into the DEMO baseline design.

Some differences between the 2021 design and the one in Ref. [97] are now discussed. The motivations to choose a 1 MeV energy of the particles, instead of 800 keV as in a previous version of the concept design [97], were that the negative impact on the availability of higher energy beam source is foreseen to be more than compensated by the RoX from ITER. Moreover, more energy means more power with the same current, and the beam current is limited by the size of the ion source and the physics of the negative ion extraction.

Regarding the choice of subdividing the beam into four horizontally separated beamlet slices with an overall square like shape (about 2 m × 1 m), instead of two longer beam slices with an overall elongated shape (about 4 m × 0.5 m) as foreseen previously [97], the main motivations are that:

- A more compact (or square-like) shape is more suitable both for a GN or a BDPN. In fact, for a GN the density distribution is more uniform with a compact shape, and for plasma neutralizers there are less plasma losses as the surface-to-volume ratio is smaller, as shown in [102].
- The fast shutter and the absolute valve adopted for the ITER NBI can be used also for DEMO NBI. This is particularly useful for the all-metal absolute valve, whose development has required large R&D and industrial efforts for the ITER HNB dimensions (1.6 m bore diameter) which is at the edge of the current state-of-the-art, as suggested by a dedicated survey in the industry. A thin-and-tall design of the NBI would have required a new and complex R&D phase to develop a new all-metal valve with almost twice the bore diameter (around 3 m).
- The main reason to adopt a two beam slices layout [97] instead of a four beam slices one was the compatibility with the photo-neutralizer that was abandoned from the DEMO baseline design due to its lack of maturity, but will be further investigated under prospective R&D in view of a future power plant after DEMO.

The main parameters of the 2021 DEMO NBI are reported in Tab. 3, where case 1 reports, for reference, the values foreseen in ITER HNB, case 2 considers the current reference design, which features an ITER-like gas neutralizer whereas case 3 considers a variation of the current design where a BDPN is considered instead of a GN. In this case, the neutralization efficiency is taken equal to 0.64, evaluated considering a degree of ionization equal to 0.1 (cf. Fig 34).

Passing from case 1 (ITER HNB) to case 2 (DEMO NBI with gas-neutralizer), a higher stripping/halo current losses efficiency (0.8 instead of 0.7, 14% higher) was assumed as a reasonable target for an optimisation of the accelerator. As a consequence, to obtain 16.67 MW per injector the needed extracted current density becomes 253 A m^{-2} instead of 289 A m^{-2} (12% lower, allowing some margin for the ion source design regarding this point of view).

The overall efficiency of the 2021 DEMO NBI is of 0.3 with a GN and 0.39 with the BDPN (considering a realistic degree of ionization γ of 0.1). If a larger degree of ionization is obtained in the BDPN (for example

Table 3
Main parameters assumed for the DEMO NBI, with a comparison to the ITER HNB.

	Case 1 ITER HNB	Case 2 2021 DEMO NBI (with GN)	Case 3 2021 DEMO NBI (with BDPN)
Fundamental requirements			
Species	H$^-$/D$^-$	D$^-$	D$^-$
Beamlet divergence	< 7 mrad	< 7 mrad	< 7 mrad
Beam on time	3600 s	7200 s	7200 s
Co-extracted electron fraction (e$^-$/D$^-$)	< 1	< 1	< 1
Required total injected power [MW]	50	50	50
Number of beamlines	3	3	3
Main design choices and related operating parameters			
Extracted D$^-$ current density [A m^{-2}]	289	253	196
Total extracted current [A]	57	50	39
Nominal acceleration voltage [kV]	1000	1000	1000
Auxiliaries/extraction overall efficiency	0.9	0.9	0.9
Gross power [MW]*	63	55	43
Stripping/halo current losses efficiency	0.7	0.8	0.8
Accelerated current [A]	40	40	31
Beam source/neutraliser entrance transmission efficiency	0.95	0.95	0.95
Neutraliser efficiency	0.55	0.55	0.71
Beam line/duct transmission efficiency	0.8	0.8	0.8
Estimated power released to the plasma per injector [MW]	16.67	16.67	16.67
Injector overall efficiency	0.26	0.30	0.39
Estimated power released to the plasma by the NBI [MW]	50	50	50

* including RF generators, cooling and pumps.

0.2 or 0.3), an even better efficiency could be obtained (see section 4.2.2).

Summarizing, the DEMO NBI functional features are close to the ones of ITER HNB, in order to better exploit the RoX from ITER, but the overall efficiency of the NBI is expected to be higher due to the on-going design optimization and R&D activities on BDPN, racetrack drivers, pumping, Cs management and beam optics. In particular, if the future R&D will demonstrate that the BDPN solution is usable in DEMO, the overall efficiency of the injector is foreseen to reach values around 0.35 or more.

4.1.3. *Description of the RAMI Analysis on the Beam Source*

In a first phase, a highly modular beam source (HMBS) design with a large number of sub-sources, (i.e. 20 negative ion sub-sources, compared to ITER with only a low modular beam sources (LMBS)) was proposed for the beam source [97]. In fact, this approach was meant to bring some advantages:

- A better alignment between the corresponding apertures of the grids, also in presence of thermal expansion, resulting in a better overall optics of the neutral beam. This is due to the fact that the modules have a significantly smaller size than the whole accelerator, hence the horizontal and vertical deformations are also reduced compared to a less modular solution.
- The R&D phase can be carried out using a small beam source, which is more flexible and less expensive than a full-size prototype. Once optimized, the sub-source can be replicated to form a cluster in the DEMO NBI.
- A better compatibility with the photo-neutralizer concept [97], which was finally not retained for the DEMO NB design.

On the other hand, there are also some drawbacks, like a more complex construction of the ion sources and of the extraction/acceleration system, which could lead to reliability and availability issues.

In order to evaluate in a systematic way the advantages and disadvantages of a highly modular design of the DEMO NBI beam source compared to an ITER-like beam source, a comparative RAMI evaluation has been carried out. It is described in Ref. [103]. Namely, two options were considered for the beam source of the DEMO NBI:

- A LMBS configuration featuring a single expansion chamber, 8 RF drivers, 3 Cs ovens and 4 segments per grid. This is similar to the beam source adopted in MITICA and ITER NBI, described in [104].
- A HMBS configuration featuring 20 beam sources, each with its RF driver and Cs oven, and 20 segments per grid. This is the beam source proposed in 2016 for DEMO NBI, described in [97].

The main conclusions of the RAMI evaluation are summarized here below:

- Considering 28 failure modes, the global Overall Score (OS) of the LMBS is 20% lower than the HMBS one. This means that the LMBS is about 20% more “RAMI compliant” than the HMBS, which is deemed marginal.
- For some failure modes, like the ones related to the Cs ovens and the water leaks, the HMBS approach brings a larger number of components and hence a higher score (i.e. more criticality). This drawback is only partially compensated by the fact that the foreseen damage to the beam source performance is reduced following the HMBS approach compared to the LMBS approach.

As a consequence, the design of the beam source for the DEMO NBI was revised by reducing the modularity from 20 to 2 ion source modules (it is 1 in ITER HNB), while the beam shape has been changed to a four slices layout (as in MITICA and ITER HNB) instead of a two slices layout, making the DEMO NBI design closer to the MITICA (or ITER HNB) one, and this benefiting from ITER RoX.

4.1.4. *Optimization of the beam line components and duct*

A strong collaboration between EUROfusion WPHCD and WPTFV (Work Package on Tritium, Fueling and Vacuum) groups has been set up in order to evaluate the heat loads on the NBI system of DEMO, with a particular focus on the beam line components and duct.

By means of an integrated suite of models developed in the WPHCD and WPTFV, all the relevant phenomena (including the pressure profiles and the corresponding pumps requirements [106]) of the beam from the accelerator exit to the tokamak first wall were simulated, by evaluating the particle trajectories in presence of electric and magnetic fields and at the same time the reactions (stripping, neutralization, re-ionization) due to the interaction of the fast particles with the background gas. The main results are the heat loads on neutralizer, residual ion dump (RID) and duct, which were used as parameters to improve the design of these components. As an example, Fig. 30 shows the final positions of the main particles in the DEMO NBI.

The main results of the updated simulations are an amount of re-ionization losses in the duct of 0.807 MW, corresponding to 4.8% of the beam power, and a peak heating power density deposited on the duct of 0.9 MW m^{-2}. These heat loads are about half the ITER ones [107] and can be exhausted using intensively cooled CuCrZr panels as a liner for the internal wall of the duct.

4.2. *R&D activities and Physics studies*

The R&D activities focus on the ion source and on concepts for improving the neutraliser efficiency. The latter can be utilised in two ways: it can either reduce the negative ion current density required to deliver the specified heating power or it can conversely be used to increase the beam power of one beam line. In either case it increases the power efficiency.

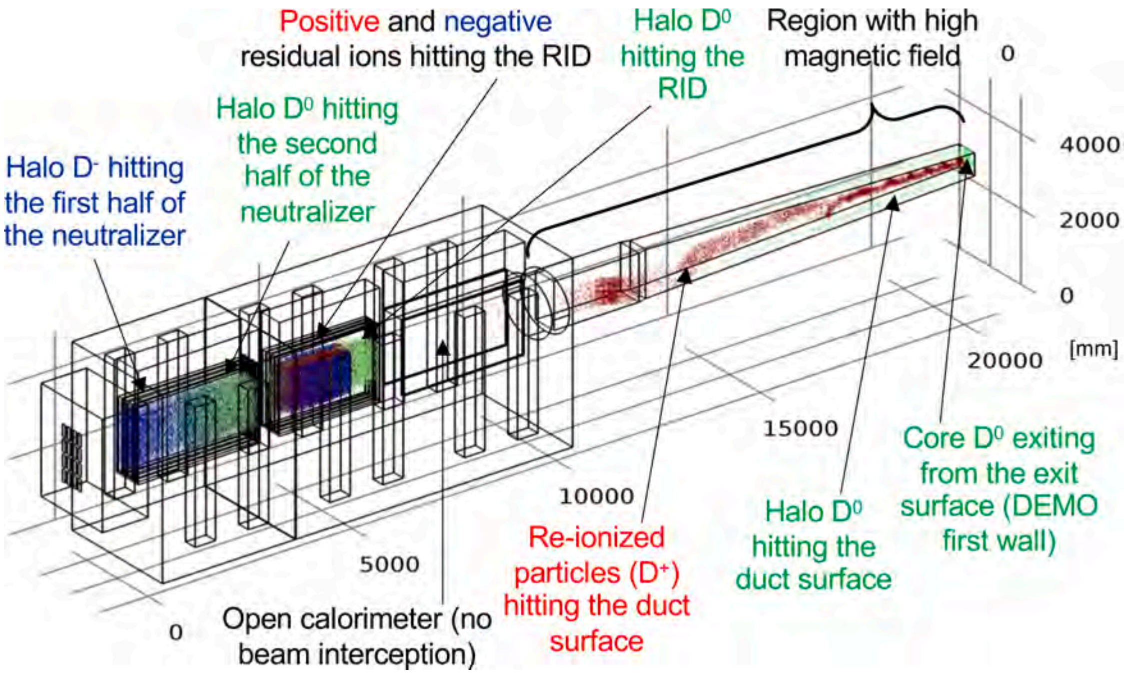

Fig. 30. Final positions of the main particles in the DEMO NBI. In blue are negative D ions, in green neutral D, and in red positive D ions. It can be observed that all residual ions (positive and negative) are effectively dumped in the residual ion dump (RID). However, other positive ions are generated by re-ionization in the duct region and they are all impinging on the duct walls due to the strong magnetic field present in the region.

4.2.1. Ion Source

Plasma generation: Modular RF drivers The concept for the ion source is based on the modular RF driver layout selected for ITER NBI where multiple RF-drivers are mounted on an expansion chamber [108,109]. In principle, any shape and size of the grid surface can be illuminated by the plasma by adapting the size of the circular drivers, their number and their arrangement. Examples are the size scaling from the prototype source to the full-size ITER source [110] or an arrangement with one column only to create a blade-shaped beam for the photo neutraliser concept [111]. Limitations, of course, come from the number and available power of the RF generators, the complexity of the RF coupling to multiple drivers and their mutual influence. State-of-the-art solid-state RF generators have already proven to facilitate the plasma matching compared to tube-based oscillators and to be more efficient without the need for water cooling [110]. Recent studies [105] at the prototype ion source with one driver and a solid-state RF generator showed that the RF power transfer efficiency ($P_{\text{plasma}}/P_{\text{generator}}$) is slightly higher for D than for H plasmas and is below 65% (Fig. 31), which means for the ITER case that more than 280 kW of the installed 800 kW power are not coupled to the plasma. Hence, coupling improvements are highly desirable. Furthermore, a strong dependence on pressure is observed, which, besides issues with plasma sustainment, makes operation at lower pressures than for the ITER sources (0.3 Pa) less attractive.

The replacement of ITER's four pairs of cylindrical drivers, each pair being series-connected to one RF generator, by four larger, racetrack-shaped drivers promises to make RF matching easier and reduce RF power consumption for similar ion source performance, as demonstrated experimentally at the prototype source [112] (cf. Figs. 4 and 5 therein). Vertical stacking of horizontally elongated drivers [110] maintains the ability to compensate vertical plasma asymmetries (attributed to plasma drifts caused by the magnetic filter field) by adjusting the RF power to each driver. A test of two racetrack drivers on the half-size ITER source is planned. Besides RF coupling, the experiments will focus on stable ion source performance over two hours in D, for which Cs management plays the crucial role.

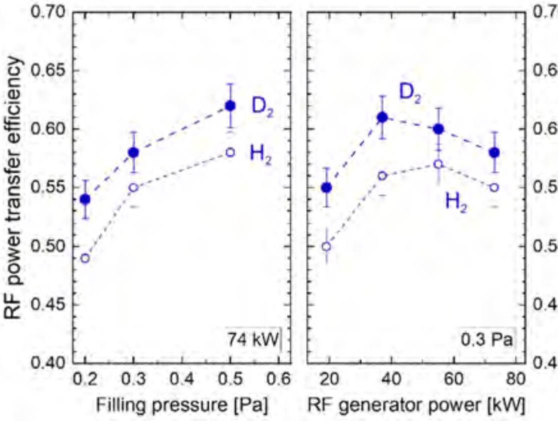

Fig. 31. RF power transfer efficiency ($P_{\text{plasma}}/P_{\text{generator}}$) measured at the prototype ion source [105].

Negative ion production: Cs management Considering the absence of a proven alternative method of producing negative ions [101] while maintaining the ratio of co-extracted electron current to ion current below one, it was decided to continue relying on Cs. Consumption and management of Cs therefore remain key questions for the DEMO NBI source. The Cs is required on the plasma grid (PG) surface where the negative ions are created and extracted. High negative ion density in front of the PG also greatly reduces the electron density and, consequently, the co-extracted electron current. In present designs Cs ovens are used to evaporate the Cs: three ovens will be mounted on the back plate of the ITER source, while the ELISE half size source hosts two ovens mounted at the side walls of the expansion chamber. The Cs coverage of the plasma grid then relies on the redistribution of the Cs by elevated source temperature, the plasma and sputtering due to the back-streaming positive ions during extraction. The Cs consumption has been estimated based on the experiments with the prototype source and the half size source (see [101] for a compilation). For H, where more data exist, a total evaporation rate of 5 mg/h results in a consumption of

100-200 g/year for the DEMO scenario. D requires even higher evaporation rates due to stronger Cs redistribution. On the other hand, the allowable rate is limited by breakdowns in the grid system caused by the Cs escaping through the grid. In fact, achieving the ITER parameters in D is still a challenge, as source operation is limited by the current of co-extracted electrons (see e.g. [101,112]), which correlates inversely with the Cs amount in front of the grid system. In long-pulse D operation the co-extracted electron current increases over time and is not uniform across the extraction area. Hence the peak power load on the extraction grid (2nd grid), where the co-extracted electrons are dumped by magnetic deflection, determines the maximum allowable RF power, extraction voltage and pulse length. So far, more than 90% of the required D current density could be demonstrated in short pulses (10 s) while only 66% were achieved in long pulses (1700 s). Thus, Cs management in deuterium is still a major challenge to overcome.

Insight into the Cs dynamics can be gained either by appropriate diagnostics or by modelling. For the latter, the Monte-Carlo code CsFlow3D, benchmarked against measurements at the prototype source, is used for predictive calculations [113]. Fig. 32 shows the simulation of 400 s pulses in the half size source and in the full size ITER source, using a total evaporation rate of 10 mg/h and 20 mg/h, respectively. The latter was adjusted such that a similar Cs flux as for the half size source is achieved. It displays a strong decrease of Cs in front of the grid. The plot shows the neutral Cs particles only, accounting for 30% of the total Cs content, while the rest is ionized. The present understanding is that Cs+ ions are less relevant for the Cs coverage of the plasma grid during plasma pulses as they are repelled by the positive bias voltage of the plasma grid [113]. Consequently, alternative evaporation concepts are under discussion, one being the Cs shower, which evaporates Cs right in front of the plasma grid, leading to reduced Cs ionisation because transport occurs only through the cold plasma boundary. The inset in Fig. 32 shows a Cs shower for the half size source, providing a low evaporation rate of 3.5 mg/h at a distance to the grid of 3 cm. The calculated neutral Cs flux, which accounts for about 70% of the total Cs flux in this case, stabilizes after depletion of other reservoirs in the source from about 50 s at a value three times higher than that with Cs ovens after 400 s. As these predictions look promising, a Cs shower has been designed for testing at the prototype source mounted at BATMAN upgrade. First indicative results are promising, but systematic studies are required. A drawback might be increased Cs leakage through the grid leading to Cs induced breakdowns. A next step could be the test on the half size source.

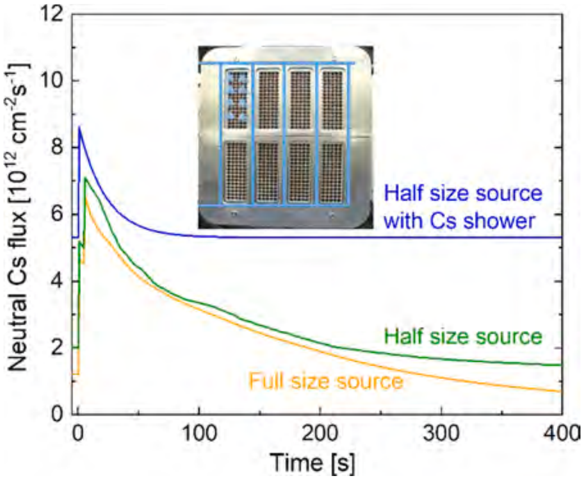

Fig. 32. Flux of neutral Cs particles onto the plasma grid during plasma operation with steady-state extraction, calculated with the code CsFlow3D [113] for the full size ITER source equipped with three ovens (6.7 mg/h each), for the half size source with two ovens (5 mg/h each) and the half size source with the Cs shower (3.5 mg/h). The arrangement of the latter is illustrated in the inlet.

Further optimisation of the ion source Among the promising options to cope with the current of co-extracted electrons is also the optimization of the magnetic filter field together with biasing particular surfaces, such as the plasma grid or dedicated additional structures. The latter can be biased segment-wise and thus counteract asymmetries in the co-extracted electrons, as latest tests at the half-size source indicate [114]. The co-extracted electron deflection field, generated by permanent magnets embedded in the second accelerator grid, extends into the plasma and also contributes to the reduction of electrons in front of the grid. Full 3D Particle-in-cell-Monte-Carlo calculations (PIC-MCC) indicate that increasing this field strongly reduces electron co-extraction. Furthermore, redesigning the second grid to tolerate higher heat loads could relax the operational limits regarding co-extracted electrons. It is recommendable that such improved designs simultaneously aim at higher transparency, reducing the required current density, and at reduced beamlet divergence in order to increase geometrical transmission and the beamline's energy efficiency. Furthermore, the magnetic field in the single apertures can be improved, so that the beamlet direction is better defined.

Reduction of stripping losses, mainly in the first gap, would also reduce the required current density and hence facilitate reliable operation. For ITER, the filling pressure of the ion source is specified as 0.3 Pa based on the expected 30% stripping losses in the seven-grid accelerator, as predicted by gas conductance calculations. For a three-stage system, as used at the half-size source, the same calculations predict about 15% losses.vs. below 10% measured losses. This difference indicates that it might be possible to work with slightly lower extracted current density or at slightly increased pressure, both of which improves the source performance in long pulses. Reducing stripping losses by reducing the pressure may still appear attractive, but one pays a price by a substantially higher and temporally increasing co-extracted electron current in combination with reduced negative ion production due to the lower particle densities in the source.

4.2.2. Neutraliser Efficiency

Beam driven Plasma Neutraliser The neutraliser is the beamline component with the highest potential for efficiency improvement, as the gas neutraliser's neutralisation yield is only ≈ 55% for 1 MeV D^-. One suggested [115] improvement is to create a plasma of sufficient degree of ionisation in the neutraliser. In collisions with electrons or ions of this neutraliser plasma the cross sections for single stripping of the fast beam ions ($D^0 \rightarrow D^0$) are larger than in collisions with neutral hydrogen, while the cross sections of D^+ forming reactions ($D^- \rightarrow D^+$, $D^0 \rightarrow D^+$) do not increase by the same factor. This increases the fraction of neutral beam atoms at the exit of the neutraliser. In the BDPN, first suggested by Surrey and Holmes [100], the plasma is generated by the passing beam itself, avoiding added system complexity.

In order to reduce the wall losses of ions and electrons and achieve the required degree of ionisation and plasma density, the neutraliser chamber is lined with cusp magnets along all boundaries, as schematically depicted in Fig. 33. For the same reason, channel separating walls like in the ITER gas neutraliser are avoided. However, as the cusp confinement at the entrance and exit requires an odd number of magnets, the horizontal separation of the beam into four beamlet groups like for the ITER beams is still a suitable layout and the beam aspect ratio of ≈ 2:1 is still appropriate to keep the surface-to-volume ratio of the BDPN chamber sufficiently low. Therefore we use a 40 A, 1 MeV D^- beam of ITER-like shape as our "ITER-like" reference case for the further discussion.

Surrey and Holmes [100] and Turner and Holmes [116] described the mechanisms of plasma generation in the BDPN and formulated a mostly zero-dimensional model that forms the basis for quantitative performance predictions. Gas ionisation is chiefly driven by the fast electrons stripped from the beam and - to a lesser extent - the

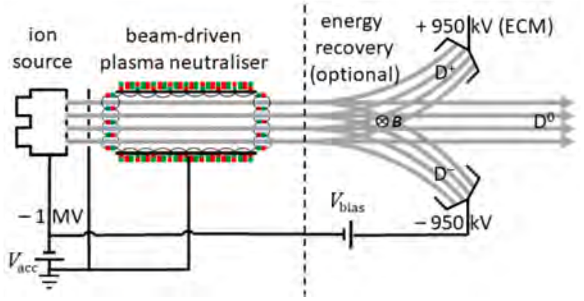

Fig. 33. Schematic of the beamline including the beam-driven plasma neutralizer (BDPN) and an optional energy recovery set-up.

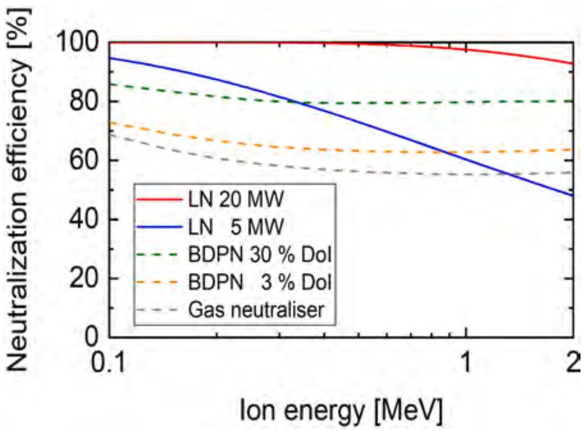

Fig. 34. Comparison of neutralisation efficiencies for a D^- beam. Dashed lines: gas neutraliser and beam-driven plasma neutraliser with 3 and 30% degree of ionisation (DoI); solid lines: laser neutraliser (LN), assuming a laser beam width of 1 cm and 5 and 20 MW of laser power.

hyperthermal electrons created through neutraliser gas ionisation in collisions with the beam ions and atoms, called Rudd electrons. The thermal electrons thus created have a low temperature of very few eV. Turner and Holmes predicted an achievable degree of ionisation of $>$ 30% and $n_e \approx 5 \times 10^{18} \mathrm{m}^{-3}$, which would lead to a neutralisation efficiency of about 80%.

The model neglects a few mechanisms that tend to decrease the plasma density. The first is the electron energy loss to dissociation of hydrogen molecules in the energy balance. Its inclusion brings down the electron temperature by a factor of two to just above 1 eV. Secondly, as the temperature of the thermal plasma electrons is so low, dissociative recombination of electrons with molecular ions becomes important [117,118]. Once formed, D_3^+ rapidly recombines dissociatively with electrons. However, the species composition and therefore the relevance of recombination turns out to be extremely sensitive to several not sufficiently known parameters and cross section values, leaving us with a wide range of predicted degrees of ionisation between about 3 and 15%. Neutralisation efficiencies for a degree of ionisation of 30% as predicted by Turner and Holmes and 3% as our lowest estimate are shown in Fig. 34 together with the efficiency of the gas neutraliser. The beam energy dependence reflects that of the involved collision cross sections.

On top of this already huge uncertainty the cusp confinement, which is crucial in achieving high plasma density, is described only by an effective loss area, neglecting any detail of the magnetic field topology such as in the corners. It should be noted that the input power density of approx. 2 kW/m^3 carried by the stripped and Rudd electrons is more than an order of magnitude below what is needed to achieve similar plasma densities in NBI ion sources. A definite answer on the concept's viability should therefore be sought from a suitable proof-of-principle experiment [118] with the main objective of investigating whether a sufficient plasma density can be obtained.

Another important aspect of a BDPN's inclusion in a beamline is the required gas flow compared with the gas neutraliser as reference. While the plasma neutraliser's lower optimal target thickness tends to decrease the gas flow, the absence of channel-separating walls increases gas conductance and flow. Furthermore, neutral gas heating due to the passing beam is more effective in the plasma neutraliser, again tendentially increasing gas throughput. We have estimated neutral gas heating [118] and find an increase by ≈ 300 K above wall temperature. Overall, the gas flow could be kept approximately the same as for the gas neutraliser by extending the magnet bars at the entrance and exit outside the cusp confined volume to reduce gas conductance.

Energy recovery Considering the uncertainties of the BDPN performance predictions, one may consider residual ion energy recovery (ER) [119] in combination with a gas neutraliser or less efficient BDPN. While ER does not increase the neutralised beam fraction and injected power, it does increase the beamline's energy efficiency by reclaiming most of the residual ions' kinetic energy. The principle is simple and depicted in Fig. 33: after the neutraliser the two polarities of residual ions are deflected out of the neutral beam in opposite direction by a transverse magnetic (or electric [120]) field. For the deceleration of the negative ions the collector electrode is connected to the potential of the ion source such that the ions arrive at (almost) zero energy and their current does not pass through the acceleration power supply. The only power invested is that by the bias power supply that applies a small voltage $V_{\text{bias}} \approx 50$ kV relative to the ion source potential, just sufficient to ensure that all ions reach the collector, as confirmed by ion trajectory simulations. The collector for the positive ions is connected to devices called Energy Conversion Modules (ECM) or Modular Resonant Converters that convert the recovered energy to useful electrical energy at the desired secondary voltage. CCFE have experimentally achieved an electrical conversion efficiency of 0.8 with test modules. Thus, up to about 95% of the residual ion power can be recovered from the negative ions and $0.95 \cdot 0.8 = 76\%$ from the positive ions.

Despite the robust principle, ER poses some considerable challenges. The large surfaces at high voltage could lead to considerable dark currents. Secondary charges [121] as well as ionised background gas in the beamline could create currents between the electrodes that would degrade the efficiency gain if no effective counter measures were taken in the design. Furthermore, the electrical connection of collector electrodes would occupy lateral space for the bushings. Lastly, ER would increase the overall beamline length by a few meters, which in turn slightly increases reionisation losses of the neutral beam and causes an integration issue with the footprint of the whole neutral beam in the nuclear zone around the tokamak.

Laser neutralizer Another possibility to increase the neutralization efficiency is by photodetachment (PD): the additional electron is detached by a high-power photon field in the neutralization region, typically provided by a laser, therefore the term *laser neutralizer (LN)*. The high power is necessary due to the rather small PD cross section and is beyond tens of MW in total for a 1 MeV negative D ion beam with ITER-like current [122–124]. Non-negligible absorption at optical components will moreover add up to significant thermal loads and possible adaptive measures have to be considered [125]. The small PD cross section also means negligible consumption of the optical power by neutralisation in a single transit. Thus, the radiation can be used multiple times, giving rise to the concepts described below. Furthermore, the low absorption of photons means that the ion beam can be large in the laser beam direction. Perpendicular to the laser beam, the diameter of the ion beam should be of the order of the laser beam width, which is typically in the range of cm. Hence, in systems using a LN it is reasonable to use ion beams with a high aspect ratio, also known as *beam sheets*. A concept in which the entire beam line including the ion source is adapted to such a design can be found in [124]. A further advantage of the laser neutraliser is the reduced gas load due to the absence of a gas target.

In Fig. 34, the neutralization efficiency for a LN, calculated following Ref. [123], is shown as a function of the ion beam energy for a 1 cm beam width. Due to the decreasing interaction time between photons and ions, the efficiency decreases with the ion energy. For 1 MeV D^- the neutralisation efficiency for a photon power of 5 MW is 60%, increasing to 97.5% for 20 MW. It has to be kept in mind that these values are valid for a 1 cm beam, i.e. for an ion beam of 5 cm width five such systems would have to be used. Another possibility is to fold the laser beam either in ion beam direction (higher neutralization rate) or perpendicular to it (larger neutralized beam section). However, for both situations the loss of optical power at the additional mirror surfaces needs to be considered.

Several concepts exist to obtain the high optical power. Inoue [122] described a system in which an array of a huge number of high-power laser diode stacks directly illuminates the ion beam (*direct drive*), which was successfully applied to negative H ion beams on much smaller scales [126]. Popov [127] uses a non-resonant *adiabatic photon trap* to obtain a comparable high-power photon field in the neutralization region. Further ideas rely on optical cavities, where Fassina [128] proposes to use the *RING concept*, in which the second harmonic of a seed laser is trapped in the cavity. A very efficient way of multiplying the laser power is by resonant systems: Kovari [123] describes the *single cavity* concept, in which the ion beam is introduced in the actual laser cavity. Thin-disc lasers mounted on one of the cavity mirrors are suggested for such a system. In contrast, Chaibi [129] proposed Fabry-Pérot (FP) cavities as *enhancement cavities* to amplify the injected laser radiation. Within WPHCD, both RING [128] and FP cavities [130,131] are studied. A schematic of both is shown in Fig. 35.

FP cavities (Fig. 35(a)) are most advanced in the context of amplification, partly due to their application for gravitational wave detectors. For Advanced LIGO for instance, an amplification of 250 and a stored laser power up to 800 kW is foreseen [132]. The seed laser is resonantly coupled into a high-finesse cavity with high reflectivity ($R > 99.9\%$) at the seed laser's wavelength. In resonance and optimal alignment, as well as neglecting absorption within the mirror substrate, the only cavity loss is given by transmission through the mirrors ($1 - R$), i.e. high amplification is possible and, thus, relatively low initial laser power is required (< 10 kW). For stable, i.e. continuous-wave resonance coupling, sophisticated locking schemes are necessary [133]. To obtain reasonable beam widths of cm, very long linear cavities (< 100 m) would be necessary. This is why these cavities are typically folded. A sophisticated concept using telescopes was presented in Ref. [134].

The RING concept (Fig. 35(b)) is based on trapping the second harmonic instead of the fundamental wavelength of the seed laser. The cavity is transmissive for the seed laser ($R \approx 5\%$) and incorporates a second harmonic generation (SHG) crystal that doubles the laser frequency. For this second harmonic the cavity mirrors are highly reflective ($R > 99.5\%$). Resonance locking is not necessary and the system is thus more robust against external influences. Furthermore, the optical design can be rather compact. However, the SHG crystal is a main source for power loss in the cavity, resulting in high thermal load on the crystal and low amplification compared with the FP concept. Hence, higher initial laser power is required (≥ 100 kW). Secondly, the concept inherently works only in pulsed operation, which means that for quasi-cw neutralization very high repetition rates ($\geq$ MHz) are necessary.

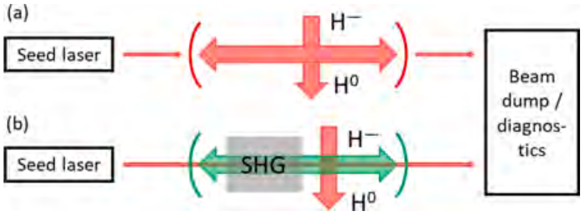

Fig. 35. Schematic of the two concepts for LN followed within WPHCD: (a) enhancement Fabry-Pérot cavity and (b) RING cavity (SHG = second harmonic generation).

The current status of both concepts is given in Table 4. Each concept needs to improve by several orders of magnitude in absolute photon power and amplification.

5. Conclusion and Perspective

During the 2014-2020 period, the WPHCD work package has advanced the design of the EC, IC and NB systems at a level expected during the PCD Phase. The designs and some R&D have to be generic in the sense that neither the physics parameters nor the machine design have reached sufficient maturity to assign definitive values for a Concept Design (CD) Phase to be followed by engineering activities.

It is foreseen that the three systems (EC, IC and NBI) will be assessed by 2024 based on their maturity and the physics needs. In order to do this, all three system designs were asked to deliver 50 MW to the plasma. However, at the beginning of 2020, a decision was made to have only EC as the baseline heating method. This decision was taken to focus resources on the system which is deemed as the closest to implementation, while still be capable of fulfilling the physics need: during the flat-top phase, all the three main functions (core heating, NTM control and thermal instability control) could be fulfilled by the injection of EC waves. Physics studies are still ongoing to determine the requirements during the ramp-up phase to estimate whether a heating which first (i.e. before thermalisation between ions and electrons) delivers the power to the ions is required. Typically, during the L-H transition, the power delivered to the ion channel is deemed of importance. During this phase, it is important to benefit from the alpha power from fusion reactions as well, and the issue of an assist to burn during this phase is being examined by physics.

With the decision to have a baseline for heating of DEMO, the programme was reorganised for the CD Phase (2021-2027). The main effort is concentrated on EC waves, with strong design activities to insure the integration into the DEMO machine. The necessary R&D will also be pursued actively, to bring the readiness and integration to sufficient levels by end of 2023. But since the physics requirements are not yet confirmed (and very likely not before 2023), heating by IC waves and NBI are considered as part of risk mitigation, in case one or both methods will be strongly required by physics findings. Naturally, due to limitations of resources, the integration effort for IC and NB cannot be pursued at the same level as for EC, but will be limited to a few selected items which are considered as essential for a decision.

For the EC wave heating, the two variants FF (using gyrotrons at fixed frequencies and a steerable mirror for NTM power deposition) and TF (using step-tunable gyrotrons to deposit the power at the NTM localisation) will be developed. These two designs shall be compatible

Table 4
Current status of the LN concepts at different institutes within the WPHCD project compared to the achieved values at Advanced LIGO and prospective values for DEMO.

Institute/ Reference	CNRS [133]	IPP [this work]	RFX [128]	Advanced LIGO [130]	DEMO
concept	FP	FP	RING	FP	
seed laser power	24 W	1.1 W used (6.2 W avail.)	nominally 300 mJ @ 10 Hz	400 W (already pre-amplifed)	≥ 1 kW
amplification	583	376	-	250	$\geq 10^3$
stability	cw	cw	200 ns	cw	cw
total	14 kW	0.4 kW	-	100 kW	≥ 10 MW

not only with the physics requirements as described in Section 2, but will also take into account their criticality and the various loads on the components (e.g. nuclear loads, electromagnetic loads during fast transients of the plasma, thermal loads from the plasma and the RF). Regarding R&D, the key points in the programme are the development of multi-frequency gyrotrons at a power level of 2 MW and operating in the range of 170-204 GHz or 136-170 GHz (Variant FF), and that of step-tunable gyrotrons for the Variant TF. For such sources, the broadband window both for the gyrotron and the tokamak entrance is a key element. Recent developments made by industry have shown that free standing diamond disks of 180 mm can be produced, and their optimisation (with respect to $\tan\delta$ will be performed. The brazing of the disc to the window structure will also be developed. Integration studies shall be one central point, with a refinement of the definition of the loads (which were not fully possible since the launcher was only defined towards the end of the programme), further work on remote maintenance and safety, and a refinement of the impact of reliability on the required installed power.

The IC antenna development will continue along the lines of the approaches described above, with the most promising TAH (toroidally arranged halves) antenna concept implying some cuts and removals of the breeder zone. These cuts shall be assessed in close collaboration with the Work Package Breeding Blanket.

For NB, the main point is naturally the design of the full system, taking as much as possible the RoX from ITER, and focusing on specifications which are different (pulse length of 7200 s compared to 3600 s requested in ITER [135], stressing the importance of Cs management and restraining the co-extracted electron current) and improvements on the RF source (RF Racetracks described above). The concept of BDPN is studied to increase the neutralisation efficiency and a possible experimental test of the creation of a plasma of suitable density is planned.

Overall, for the three HCD systems, a comprehensive programme with different degrees of integration was prepared. It will allow for EC to move to a concept design in up to end of 2023. For IC and NB, the key elements for an inclusion as baseline heating methods will be available, if demanded by the DEMO physics team.

CRediT authorship contribution statement

M.Q. Tran: Project administration, Supervision, Writing – original draft, Writing – review & editing. **P. Agostinetti:** Project administration, Supervision, Writing – original draft, Writing – review & editing. **G. Aiello:** Investigation, Methodology, Software, Validation. **K. Avramidis:** Investigation, Methodology, Software, Validation. **B. Baiocchi:** Investigation, Methodology, Software, Validation. **M. Barbisan:** Investigation, Methodology, Software, Validation. **V. Bobkov:** Project administration, Supervision, Writing – original draft, Writing – review & editing. **S. Briefi:** Writing – review & editing, Investigation, Methodology, Software, Validation. **A. Bruschi:** Project administration, Supervision, Writing – original draft, Writing – review & editing. **R. Chavan:** Investigation, Methodology, Software, Validation. **I. Chelis:** Investigation, Methodology, Software, Validation. **Ch. Day:** Conceptualization. **R. Delogu:** Investigation, Methodology, Software, Validation. **B. Ell:** Investigation, Methodology, Software, Validation. **F. Fanale:** Investigation, Methodology, Software, Validation. **A. Fassina:** Investigation, Methodology, Software, Validation. **U. Fantz:** Project administration, Supervision, Writing – original draft, Writing – review & editing. **H. Faugel:** Investigation, Methodology, Software, Validation. **L. Figini:** Investigation, Methodology, Software, Validation. **D. Fiorucci:** Investigation, Methodology, Software, Validation. **R. Friedl:** Investigation, Methodology, Software, Validation. **Th. Franke:** Investigation, Methodology, Software, Validation. **G. Gantenbein:** Investigation, Methodology, Software, Validation. **S. Garavaglia:** Investigation, Methodology, Software, Validation. **G. Granucci:** Investigation, Methodology, Software, Validation. **S. Hanke:** Investigation, Methodology, Software, Validation. **J.-P. Hogge:** Writing – review & editing, Visualization. **C. Hopf:** Writing – review & editing, Investigation, Methodology, Software, Validation. **A. Kostic:** Investigation, Methodology, Software, Validation. **S. Illy:** Investigation, Methodology, Software, Validation. **Z. Ioannidis:** Investigation, Methodology, Software, Validation. **J. Jelonnek:** Project administration, Supervision, Writing – original draft, Writing – review & editing. **J. Jin:** Investigation, Methodology, Software, Validation. **G. Latsas:** Investigation, Methodology, Software, Validation. **F. Louche:** Investigation, Methodology, Software, Validation. **V. Maquet:** Investigation, Methodology, Software, Validation. **R. Maggiora:** Investigation, Methodology, Software, Validation. **A. Messiaen:** Investigation, Methodology, Software, Validation. **D. Milanesio:** Investigation, Methodology, Software, Validation. **A. Mimo:** Investigation, Methodology, Software, Validation. **A. Moro:** Investigation, Methodology, Software, Validation. **R. Ochoukov:** Investigation, Methodology, Software, Validation. **J. Ongena:** Project administration, Supervision, Writing – original draft, Writing – review & editing. **I.G. Pagonakis:** Investigation, Methodology, Software, Validation. **D. Peponis:** Investigation, Methodology, Software, Validation. **A. Pimazzoni:** Investigation, Methodology, Software, Validation. **R. Ragona:** Investigation, Methodology, Software, Validation. **N. Rispoli:** Investigation, Methodology, Software, Validation. **T. Ruess:** Investigation, Methodology, Software, Validation. **T. Rzesnicki:** Investigation, Methodology, Software, Validation. **T. Scherer:** Investigation, Methodology, Software, Validation. **P. Spaeh:** Investigation, Methodology, Software, Validation. **G. Starnella:** Investigation, Methodology, Software, Validation. **D. Strauss:** Project administration, Supervision, Writing – original draft, Writing – review & editing. **M. Thumm:** Investigation, Methodology, Software, Validation. **W. Tierens:** Investigation, Methodology, Software, Validation. **I. Tigelis:** Investigation, Methodology, Software, Validation. **C. Tsironis:** Investigation, Methodology, Software, Validation. **M. Usoltceva:** Investigation, Methodology, Software, Validation. **D. Van Eester:** Investigation, Methodology, Software, Validation. **F. Veronese:** Investigation, Methodology, Software, Validation. **P. Vincenzi:** Investigation, Methodology, Software, Validation. **F. Wagner:** Conceptualization. **C. Wu:** Investigation, Methodology, Software, Validation. **F. Zeus:** Investigation, Methodology, Software, Validation. **W. Zhang:** Investigation, Methodology, Software, Validation.

Declaration of Competing Interest

The authors declare that they have no known competing financial interests or personal relationships that could have appeared to influence the work reported in this paper

Acknowledgement

This work has been carried out within the framework of the EUROfusion Consortium, funded by the European Union via the Euratom Research and Training Programme (Grant Agreement No 101052200 - EUROfusion). Views and opinions expressed are however those of the author(s) only and do not necessarily reflect those of the European Union or the European Commission. Neither the European Union nor the European Commission can be held responsible for them.

References

[1] M. Siccinio, W. Biel, E. Fable, T. Franke, F. Janky, P. Lang, M. Mattei, F. Maviglia, F. Palermo, O. Sauter, M. Tran, S. Van Mulders, H. Zohm, Impact of the plasma operation on the technical requirements in eu-demo, Fusion Engineering and Design 179 (2022) 113123, https://doi.org/10.1016/j.fusengdes.2022.113123.

[2] M. Tran, HCD SRD for FP9, V2.0. Technical Report, 2020.

[3] E. Poli, A. Bock, M. Lochbrunner, O. Maj, M. Reich, A. Snicker, A. Stegmeir, F. Volpe, N. Bertelli, R. Bilato, G. Conway, D. Farina, F. Felici, L. Figini, R. Fischer, C. Galperti, T. Happel, Y. Lin-Liu, N. Marushchenko, U. Mszanowski, F. Poli, J. Stober, E. Westerhof, R. Zille, A. Peeters, G. Pereverzev, TORBEAM 2.0, a paraxial beam tracing code for electron-cyclotron beams in fusion plasmas for

extended physics applications, Computer Physics Communications 225 (2018) 36–46, https://doi.org/10.1016/j.cpc.2017.12.018.

[4] D. Farina, A Quasi-Optical Beam-Tracing Code for Electron Cyclotron Absorption and Current Drive: GRAY, Fusion Science and Technology 52 (2) (2007) 154–160, https://doi.org/10.13182/FST07-A1494.

[5] S. Garavaglia, B. Baiocchi, A. Bruschi, A. Čufar, F. Fanale, G. Granucci, A. Moro, E. Poli, N. Rispoli, T. Scherer, M. Siccinio, P. Späh, D. Strauß, I. Tigelis, C. Tsironis, T. Franke, M.Q. Tran, EU DEMO EC equatorial launcher pre-conceptual performance studies, Fusion Engineering and Design 156 (2020) 111594, https://doi.org/10.1016/j.fusengdes.2020.111594.

[6] DEMO1 Reference Design - 2018, Technical Report, 2018.

[7] M.Q. Tran, Datasheet for Electron Cyclotron System with Fixed Frequency, v1.2. Technical Report, 2020.

[8] M.Q. Tran, Datasheet for Electron Cyclotron System with Tunable Frequency, v1.2. Technical Report, 2020.

[9] B.Baiocchi, ECRH and ECCD modeling studies for DEMO scenarios. 47th EPS Conference on Plasma Physics volume 45A, 2021.Sitges, Spain

[10] A. Snicker, ECCD Turbulence interaction in DEMO, v1.1. Technical Report, 2020.

[11] A. Bruschi, HCD-4.1.06-T018, Final Report on Deliverables D001,-D002,-D003,-D004,-D005, v1.0. Technical Report, 2020.

[12] M. Siccinio, Plasma current and toroidal field direction in DEMO, v1.0. Technical Report, 2020.

[13] T. Franke, G. Aiello, K. Avramidis, C. Bachmann, B. Baiocchi, C. Baylard, A. Bruschi, D. Chauvin, A. Cufar, R. Chavan, C. Gliss, F. Fanale, L. Figini, G. Gantenbein, S. Garavaglia, G. Granucci, J. Jelonnek, G.S. López, A. Moro, M. Moscheni, N. Rispoli, M. Siccinio, P. Spaeh, D. Strauss, F. Subba, I. Tigelis, M. Tran, C. Tsironis, C. Wu, H. Zohm, Integration concept of an Electron Cyclotron System in DEMO, Fusion Engineering and Design 168 (2021) 112653, https://doi.org/10.1016/j.fusengdes.2021.112653.

[14] R. Chavan, Pre-conceptual design of an actuator system for the EC mid steering antenna (MSA), v1.5. Technical Report, 2021.

[15] P. Spaeh, C. Bachmann, R. Chavan, A. Cufar, T. Franke, D. Strauss, M.Q. Tran, Structural pre-conceptual design studies for an EU DEMO equatorial EC port plug and its port integration, Fusion Engineering and Design 161 (2020) 111885, https://doi.org/10.1016/j.fusengdes.2020.111885.

[16] E. Flynn, RM-3.5.1-T001-PD29-Electron Cyclotron technical support, design development and maintenance integration, V1.0. Technical Report, 2021.

[17] V. Erckmann, W. Kasparek, G. Gantenbein, F. Hollmann, L. Jonitz, F. Noke, F. Purps, M. Weissgerber, W7-X ECRH Teams at IPP Greifswald, FZK Karlsruhe, IPF Stuttgart, ECRH for W7-X: Transmission Losses of High-Power 140-GHz Wave Beams, Fusion Science and Technology 55 (1) (2009) 16–22, https://doi.org/10.13182/FST09-A4049.

[18] S. Garavaglia, G. Aiello, S. Alberti, K. Avramidis, A. Bruschi, I.G. Chelis, J. Franck, G. Gantenbein, G. Granucci, G. Grossetti, K. Hizanidis, S. Illy, J. Jelonnek, P. Kalaria, G. Latsas, A. Moro, I. Pagonakis, D.V. Peponis, E. Poli, N. Rispoli, S. Ruess, T. Rzesnicki, T. Scherer, D. Strauss, M. Thumm, I. Tigelis, C. Tsironis, C. Wu, T. Franke, M.Q. Tran, EU DEMO EC system preliminary conceptual design, Fusion Engineering and Design 136 (2018) 1173–1177, https://doi.org/10.1016/j.fusengdes.2018.04.097.

[19] M. Thumm, State-of-the-Art of High-Power Gyro-Devices and Free Electron Masers, Journal of Infrared, Millimeter, and Terahertz Waves 41 (1) (2020) 1–140, https://doi.org/10.1007/s10762-019-00631-y.

[20] M. Thumm, G. Denisov, K. Sakamoto, M. Tran, High-power gyrotrons for electron cyclotron heating and current drive, Nuclear Fusion 59 (7) (2019) 073001, https://doi.org/10.1088/1741-4326/ab2005.

[21] H. Jory, CPI Gyrotrons For Fusion EC Heating. AIP Conference Proceedings volume 807, AIP, Kalamata (Greece), 2006, pp. 180–190, https://doi.org/10.1063/1.2158773. http://aip.scitation.org/doi/abs/10.1063/1.2158773.ISSN: 0094243X

[22] M. Blank, P. Borchard, S. Cauffman, K. Felch, Development and demonstration of a 900 kW, 140 GHz gyrotron. 2015 IEEE International Vacuum Electronics Conference (IVEC), IEEE, Beijing, China, 2015, pp. 1–2, https://doi.org/10.1109/IVEC.2015.7223747. http://ieeexplore.ieee.org/document/7223747/.

[23] A. Kumar, N. Kumar, U. Singh, R. Bhattacharya, V. Yadav, A. Sinha, Towards a 1MW, 170GHz gyrotron design for fusion application, Infrared Physics & Technology 57 (2013) 1–7, https://doi.org/10.1016/j.infrared.2012.11.006.

[24] B. Liu, J. Feng, Y. Zhang, Y. Zhang, B. Chen, Study of 140GHz and 170GHz gyrotrons for fusion plasma ECRH. 2019 International Vacuum Electronics Conference (IVEC), IEEE, Busan, Korea (South), 2019, pp. 1–2, https://doi.org/10.1109/IVEC.2019.8744858. https://ieeexplore.ieee.org/document/8744858/.

[25] G.-W. Wu, Design of a TE34,10 mode cylindrical cavity for MW level gyrotron, Journal of Infrared and Millimeter Waves 38 (2019).

[26] Y.-h. Liu, C. Lei, X.-j. Niu, H. Wang, G. Guo, S. Zhang, H. Li, Study and design of cavity and MIG of a high-power, 140 GHz gyrotron at UESTC, Physics of Plasmas 26 (3) (2019) 033106, https://doi.org/10.1063/1.5088005.

[27] L. Hu, G. Ma, D. Sun, Q. Huang, T. Zhuo, S. Gong, Y. Jiang, Z. Zeng, Q. Ma, W. Lei, R. Song, P. Hu, X. Hu, Z. Guo, X. Ku, Z. Tan, H. Chen, F. Meng, Development of a 28-GHz/50-kW/30-s Gyrotron System for Fusion Application, IEEE Transactions on Plasma Science 49 (4) (2021) 1468–1474, https://doi.org/10.1109/TPS.2021.3066553.

[28] J. Jelonnek, G. Aiello, S. Alberti, K. Avramidis, F. Braunmueller, A. Bruschi, J. Chelis, J. Franck, T. Franke, G. Gantenbein, S. Garavaglia, G. Granucci, G. Grossetti, S. Illy, Z. Ioannidis, J. Jin, P. Kalaria, G. Latsas, I. Pagonakis, T. Rzesnicki, S. Ruess, T. Scherer, M. Schmid, D. Strauss, C. Wu, I. Tigelis, M. Thumm, M. Tran, Design considerations for future DEMO gyrotrons: A review on related gyrotron activities within EUROfusion, Fusion Engineering and Design 123 (2017) 241–246, https://doi.org/10.1016/j.fusengdes.2017.01.047.

[29] K.A. Avramidis, G. Aiello, S. Alberti, P.T. Brücker, A. Bruschi, I. Chelis, T. Franke, G. Gantenbein, S. Garavaglia, J. Genoud, M. George, G. Granucci, G. Grossetti, J.-P. Hogge, S. Illy, Z.C. Ioannidis, J. Jelonnek, J. Jin, P.C. Kalaria, G.P. Latsas, A. Marek, I.G. Pagonakis, D.V. Peponis, S. Ruess, T. Ruess, T. Rzesnicki, T. Scherer, M. Schmid, D. Strauss, M. Thumm, I. Tigelis, C. Wu, A. Zein, A. Zisis, M.Q. Tran, Overview of recent gyrotron R&D towards DEMO within EUROfusion Work Package Heating and Current Drive, Nuclear Fusion 59 (6) (2019) 066014, https://doi.org/10.1088/1741-4326/ab12f9.

[30] B. Piosczyk, G. Dammertz, O. Dumbrajs, O. Drumm, S. Illy, J. Jin, M. Thumm, A 2-MW, 170-GHz Coaxial Cavity Gyrotron, IEEE Transactions on Plasma Science 32 (2) (2004) 413–417, https://doi.org/10.1109/TPS.2004.827605.

[31] J. Franck, Systematic Study of Key Components for a Coaxial-Cavity Gyrotron for DEMO, 2017, https://doi.org/10.5445/KSP/1000068000. https://publikationen.bibliothek.kit.edu/1000068000.Medium: PDF Publisher: KIT Scientific Publishing

[32] P.C. Kalaria, Feasibility and Operational Limits for a 236 GHz Hollow-Cavity Gyrotron for DEMO, 2017, https://doi.org/10.5445/KSP/1000073581. https://publikationen.bibliothek.kit.edu/1000073581.Medium: PDF Publisher: KIT Scientific Publishing

[33] T. Rzesnicki, B. Piosczyk, S. Kern, S. Illy, Jianbo Jin, A. Samartsev, A. Schlaich, M. Thumm, 2.2-MW Record Power of the 170-GHz European Preprototype Coaxial-Cavity Gyrotron for ITER, IEEE Transactions on Plasma Science 38 (6) (2010) 1141–1149, https://doi.org/10.1109/TPS.2010.2040842.

[34] S. Ruess, J. Jelonnek, M.-Q. Tran, Pushing the KIT 2 MW Coaxial-Cavity Short-Pulse Gyrotron Towards a DEMO Relevant Design, 2020, ISBN: 9783731510246 OCLC: 1242723456.

[35] Z.C. Ioannidis, T. Rzesnicki, K.A. Avramidis, G. Gantenbein, S. Illy, J. Jin, L. Krier, I.G. Pagonakis, S. Ruess, M. Schmid, M. Thumm, J. Jelonnek, Operation of the Modular KIT 170 GHz – 2 MW Longer-Pulse Coaxial-Cavity Gyrotron with Pulses up to 50 ms. 2020 45th International Conference on Infrared, Millimeter, and Terahertz Waves (IRMMW-THz), IEEE, Buffalo, NY, USA, 2020, pp. 01–02, https://doi.org/10.1109/IRMMW-THz46771.2020.9370698. https://ieeexplore.ieee.org/document/9370698/.

[36] P.C. Kalaria, M. George, S. Uly, K.A. Avramidis, G. Gantenbein, S. Ruess, T. Rzesnicki, M. Thumm, J. Jelonnek, Performance analysis of an insert cooling system for long-pulse operation of a coaxial-cavity gyrotron. 2018 IEEE International Vacuum Electronics Conference (IVEC), IEEE, Monterey, CA, 2018, pp. 69–70, https://doi.org/10.1109/IVEC.2018.8391556. https://ieeexplore.ieee.org/document/8391556/.

[37] P.C. Kalaria, M. George, S. Illy, K.A. Avramidis, G. Gantenbein, S. Ruess, M. Thumm, J. Jelonnek, Multiphysics Modeling of Insert Cooling System for a 170-GHz, 2-MW Long-Pulse Coaxial-Cavity Gyrotron, IEEE Transactions on Electron Devices 66 (9) (2019) 4008–4015, https://doi.org/10.1109/TED.2019.2928222.

[38] S. Illy, K.A. Avramidis, P.T. Brucker, G. Gantenbein, P.C. Kalaria, S. Ruess, M. Thumm, J. Jelonnek, Investigation of a Mini-Channel Cavity Cooling Concept for a 170 GHz, 2 MW Coaxial-Cavity Gyrotron. 2019 44th International Conference on Infrared, Millimeter, and Terahertz Waves (IRMMW-THz), IEEE, Paris, France, 2019, pp. 1–2, https://doi.org/10.1109/IRMMW-THz.2019.8874446. https://ieeexplore.ieee.org/document/8874446/.

[39] Z.C. Ioannidis, I. Chelis, G. Gantenbein, T. Rzesnicki, J. Jelonnek, Experimental Classification and Enhanced Suppression of Parasitic Oscillations in Gyrotron Beam Tunnels, IEEE Transactions on Electron Devices 67 (12) (2020) 5783–5789, https://doi.org/10.1109/TED.2020.3025751.

[40] I.G. Pagonakis, K.A. Avramidis, G. Gantenbein, S. Illy, Z.C. Ioannidis, J. Jin, P. Kalaria, B. Piosczyk, S. Ruess, T. Ruess, T. Rzesnicki, M. Thumm, J. Jelonnek, Triode magnetron injection gun for the KIT 2 MW 170 GHz coaxial cavity gyrotron, Physics of Plasmas 27 (2) (2020) 023105, https://doi.org/10.1063/1.5132615.

[41] S. Ruess, I.G. Pagonakis, G. Gantenbein, S. Illy, T. Kobarg, T. Rzesnicki, M. Thumm, J. Weggen, J. Jelonnek, An Inverse Magnetron Injection Gun for the KIT 2-MW Coaxial-Cavity Gyrotron, IEEE Transactions on Electron Devices 63 (5) (2016) 2104–2109, https://doi.org/10.1109/TED.2016.2540298.

[42] S. Ruess, G. Gantenbein, S. Illy, T. Kobarg, I.G. Pagonakis, T. Rzesnicki, M. Thumm, J. Weggen, J. Jelonnek, Tolerance Studies on an Inverse Magnetron Injection Gun for a 2-MW 170-GHz Coaxial-Cavity Gyrotron, IEEE Transactions on Electron Devices 64 (9) (2017) 3870–3876, https://doi.org/10.1109/TED.2017.2723160.

[43] I. Pagonakis, J.-P. Hogge, S. Alberti, K. Avramides, J. Vomvoridis, A New Concept for the Collection of an Electron Beam Configured by an Externally Applied Axial Magnetic Field, IEEE Transactions on Plasma Science 36 (2) (2008) 469–480, https://doi.org/10.1109/TPS.2008.917943.

[44] C. Wu, Conceptual Studies of Multistage Depressed Collectors for Gyrotrons, 2019, https://doi.org/10.5445/KSP/1000094598. https://publikationen.bibliothek.kit.edu/1000094598.Medium: PDF Publisher: KIT Scientific Publishing

[45] B. Ell, Mechanical Design of the Short Pulse EB Drift Two-Stage Depressed Collector Prototype for High Power Gyrotron. 2021 22nd International Vacuum Electronics, Conference (IVEC), 2021.Rotterdam

[46] K. Sakamoto, K. Kajiwara, Y. Oda, K. Takahashi, K. Hayashi, N. Kobayashi, Progress of high power multi-frequency gyrotron development. 2012 37th International Conference on Infrared, Millimeter, and Terahertz Waves, IEEE, Wollongong, NSW, Australia, 2012, pp. 1–3, https://doi.org/10.1109/IRMMW-THz.2012.6380240. http://ieeexplore.ieee.org/document/6380240/.

[47] R. Ikeda, Y. Oda, T. Kobayashi, M. Terakado, K. Kajiwara, K. Takahashi, S. Moriyama, K. Sakamoto, Development of multi-frequency gyrotron for ITER and DEMO at QST. 2016 41st International Conference on Infrared, Millimeter, and Terahertz waves (IRMMW-THz), IEEE, Copenhagen, Denmark, 2016, pp. 1–2, https://doi.org/10.1109/IRMMW-THz.2016.7758384. http://ieeexplore.ieee.org/document/7758384/.

[48] D. Wagner, J. Stober, M. Kircher, F. Leuterer, F. Monaco, M. Munich, M. Schubert, H. Zohm, G. Gantenbein, J. Jelonnek, M. Thumm, A. Meier, T. Scherer, D. Strauss, W. Kasparek, C. Lechte, B. Plaum, A. Zach, A. Litvak, G. Denisov, A. Chirkov, L. Popov, V. Nichiporenko, V. Myasnikov, E. Tai, E. Solyanova, S. Malygin, Commissioning of the extended multi-frequency ECRH system at ASDEX upgrade. 2017 42nd International Conference on Infrared, Millimeter, and Terahertz Waves (IRMMW-THz), IEEE, Cancun, Mexico, 2017, pp. 1–2, https://doi.org/10.1109/IRMMW-THz.2017.8067025. http://ieeexplore.ieee.org/document/8067025/.

[49] J.-P. Hogge, S. Alberti, K.A. Avramidis, A. Bruschi, W. Bin, F. Cau, F. Cismondi, J. Dubray, D. Fasel, G. Gantenbein, S. Garavaglia, J. Genoud, T.P. Goodman, S. Illy, J. Jin, F. Legrand, R. Marchesin, B. Marlétaz, J. Masur, A. Moro, C. Moura, I.G. Pagonakis, E. Périal, L. Savoldi, T. Scherer, U. Siravo, M. Thumm, M. Toussaint, M.-Q. Tran, Megawatt power generation of the dual-frequency gyrotron for TCV at 84 and 126 GHz, in long pulses, 2020, p. 090006, https://doi.org/10.1063/5.0014343. http://aip.scitation.org/doi/abs/10.1063/5.0014343. Yogyakarta, Indonesia

[50] J. Franck, S. Illy, K.A. Avramidis, J. Jelonnek, M. Thumm, Mode selection and resonator design for DEMO gyrotrons. IEEE International Vacuum Electronics Conference, IEEE, Monterey, CA, USA, 2014, pp. 31–32, https://doi.org/10.1109/IVEC.2014.6857475. http://ieeexplore.ieee.org/document/6857475/.

[51] T. Ruess, K. Avramidis, G. Gantenbein, S. Illy, Z. Ioannidis, J. Jin, P. Kalaria, I. G. Pagonakis, S. Ruess, T. Rzesnicki, M. Thumm, J. Jelonnek, Theoretical Study on the Operation of the EU/KIT TE34,19-Mode Coaxial-Cavity Gyrotron at 170/204/238 GHz, EPJ Web of Conferences 203 (2019) 04014, https://doi.org/10.1051/epjconf/201920304014.

[52] T. Ruess, K.A. Avramidis, G. Gantenbein, Z. Ioannidis, S. Illy, J. Jin, F.C. Lutz, I. G. Pagonakis, S. Ruess, T. Rzesnick, M. Thumm, D. Wagner, J. Jelonnek, Operating the KIT 170 GHz 2 MW Coaxial-Cavity Gyrotron at 204 GHz: Performance Expectations and First Cold Test of the Quasi-Optical System. 2019 International Vacuum Electronics Conference (IVEC), IEEE, Busan, Korea (South), 2019, pp. 1–2, https://doi.org/10.1109/IVEC.2019.8745094. https://ieeexplore.ieee.org/document/8745094/.

[53] T. Ruess, Performance Expectation and Preparation of the First Experimental Campaign of the EU/KIT 2 MW 170/204 GHz Coaxial-Cavity Gyrotron, 2021. Rotterdam

[54] M. Schmid, J. Franck, P. Kalaria, K. Avramidis, G. Gantenbein, S. Illy, J. Jelonnek, I.G. Pagonakis, T. Rzesnicki, M. Thumm, Gyrotron development at KIT: FULGOR test facility and gyrotron concepts for DEMO, Fusion Engineering and Design 96-97 (2015) 589–592, https://doi.org/10.1016/j.fusengdes.2015.03.003.

[55] M. Thumm, A. Arnold, E. Borie, O. Braz, G. Dammertz, O. Dumbrajs, K. Koppenburg, M. Kuntze, G. Michel, B. Piosczyk, Frequency step-tunable (114–170 GHz) megawatt gyrotrons for plasma physics applications, Fusion Engineering and Design 53 (1-4) (2001) 407–421, https://doi.org/10.1016/S0920-3796(00)00519-6.

[56] H. Zohm, M. Thumm, On the use of step-tuneable gyrotrons in ITER, Journal of Physics: Conference Series 25 (2005) 274–282, https://doi.org/10.1088/1742-6596/25/1/033.

[57] D. Wagner, F. Leuterer, A. Manini, F. Monaco, M. Münich, F. Ryter, H. Schütz, H. Zohm, T. Franke, R. Heidinger, M. Thumm, W. Kasparek, G. Gantenbein, A. G. Litvak, L.G. Popov, V.O. Nichiporenko, V.E. Myasnikov, G.G. Denisov, E. M. Tai, E.A. Solyanova, S.A. Malygin, NEW FREQUENCY STEP-TUNABLE ECRH SYSTEM FOR ASDEX UPGRADE, International Journal of Infrared and Millimeter Waves 27 (2) (2007) 173–182, https://doi.org/10.1007/s10762-006-9021-y.

[58] G. Gantenbein, A. Samartsev, G. Aiello, G. Dammertz, J. Jelonnek, M. Losert, A. Schlaich, T.A. Scherer, D. Strauss, M. Thumm, D. Wagner, First Operation of a Step-Frequency Tunable 1-MW Gyrotron With a Diamond Brewster Angle Output Window, IEEE Transactions on Electron Devices 61 (6) (2014) 1806–1811, https://doi.org/10.1109/TED.2013.2294739.

[59] A. Samartsev, K.A. Avramidis, G. Gantenbein, G. Dammertz, M. Thumm, J. Jelonnek, Efficient Frequency Step-Tunable Megawatt-Class D -Band Gyrotron, IEEE Transactions on Electron Devices 62 (7) (2015) 2327–2332, https://doi.org/10.1109/TED.2015.2433016.

[60] T. Ruess, K.A. Avramidis, G. Gantenbein, S. Illy, T. Rzesnicki, M. Thumm, J. Jelonnek, Theoretical Study on the Possibility for Stepwise Tuning of the Frequency of the KIT 2 MW 170/204 GHz Coaxial-Cavity Gyrotron. 2020 45th International Conference on Infrared, Millimeter, and Terahertz Waves (IRMMW-THz), IEEE, Buffalo, NY, USA, 2020, pp. 1–2, https://doi.org/10.1109/IRMMW-THz46771.2020.9370801. https://ieeexplore.ieee.org/document/9370801/.

[61] T. Ruess, K.A. Avramidis, G. Gantenbein, S. Illy, Z. Ioannidis, P. Kalaria, M. Obermaier, I.G. Pagonakis, S. Ruess, T. Rzesnicki, M. Thumm, J. Jelonnek, Considerations on the selection of operating modes for future coaxial-cavity gyrotrons for DEMO. 2018 11th German Microwave Conference (GeMiC), IEEE, Freiburg, Germany, 2018, pp. 283–286, https://doi.org/10.23919/GEMIC.2018.8335085. http://ieeexplore.ieee.org/document/8335085/.

[62] Diamond Materials GmbH, Freiburg, Germany, https://www.diamond-materials.com/en/.

[63] G. Aiello, S. Schreck, K. Avramidis, T. Franke, G. Gantenbein, J. Jelonnek, A. Meier, T. Scherer, D. Strauss, M. Thumm, M. Tran, C. Wild, E. Woerner, Towards large area CVD diamond disks for Brewster-angle windows, Fusion Engineering and Design 157 (2020) 111818, https://doi.org/10.1016/j.fusengdes.2020.111818.

[64] G. Aiello, K.A. Avramidis, T. Franke, G. Gantenbein, J. Jelonnek, A. Meier, T. Scherer, S. Schreck, D. Strauss, M. Thumm, M.Q. Tran, C. Wild, E. Woerner, Large Area Diamond Disk Growth Experiments and Thermomechanical Investigations for the Broadband Brewster Window in DEMO, IEEE Transactions on Electron Devices 68 (9) (2021) 4669–4674, https://doi.org/10.1109/TED.2021.3088077.

[65] M. Usoltceva, V. Bobkov, H. Faugel, T. Franke, A. Kostic, R. Maggiora, D. Milanesio, V. Maquet, R. Ochoukov, W. Tierens, F. Zeus, W. Zhang, DEMO ion cyclotron heating: Status of ITER-type antenna design, Fusion Engineering and Design 165 (2021) 112269, https://doi.org/10.1016/j.fusengdes.2021.112269.

[66] V. Bobkov, M. Usoltceva, H. Faugel, A. Kostic, R. Maggiora, D. Milanesio, V. Maquet, R. Ochoukov, W. Tierens, F. Zeus, W. Zhang, Development of pre-conceptual ITER-type ICRF antenna design for DEMO, Nuclear Fusion 61 (4) (2021) 046039, https://doi.org/10.1088/1741-4326/abe7d0.

[67] W. Zhang, R. Bilato, T. Lunt, A. Messiaen, R. Pitts, S. Lisgo, X. Bonnin, V. Bobkov, D. Coster, Y. Feng, P. Jacquet, J. Noterdaeme, Scrape-off layer density tailoring with local gas puffing to maximize ICRF power coupling in ITER, Nuclear Materials and Energy 19 (2019) 364–371, https://doi.org/10.1016/j.nme.2018.12.025.

[68] V. Maquet, A. Messiaen, Optimized phasing conditions to avoid edge mode excitation by ICRH antennas, Journal of Plasma Physics 86 (6) (2020) 855860601, https://doi.org/10.1017/S0022377820001415.

[69] A. Messiaen, R. Koch, R. Weynants, P. Dumortier, F. Louche, R. Maggiora, D. Milanesio, Performance of the ITER ICRH system as expected from TOPICA and ANTITER II modelling, Nuclear Fusion 50 (2) (2010) 025026, https://doi.org/10.1088/0029-5515/50/2/025026.

[70] A. Messiaen, D. Swain, M. Vervier, P. Dumortier, F. Durodié, D. Grine, Influence of the plasma profile and the antenna geometry on the matching and current distribution control of the ITER ICRF antenna array. Optimization of the decoupling-matching system, Fusion Engineering and Design 88 (6-8) (2013) 501–506, https://doi.org/10.1016/j.fusengdes.2013.01.030.

[71] D. Grine, M. Vervier, A. Messiaen, P. Dumortier, Implementation on a mock-up of the automatic feedback controlled matching options of the full ITER ICRH system, Fusion Engineering and Design 86 (6-8) (2011) 978–981, https://doi.org/10.1016/j.fusengdes.2011.01.092.

[72] V. Maquet, V. Bobkov, A. Messiaen, M. Usoltceva, Preliminary RF characterization of DEMO in-port ion cyclotron heating system for toroidal and poloidal geometry variations, Fusion Engineering and Design 169 (2021) 112508, https://doi.org/10.1016/j.fusengdes.2021.112508.

[73] L. Colas, A. Argouarch, S. Brémond, M. Chantant, Y. Corre, M. Firdaouss, M. Goniche, D. Guilhem, J.-P. Gunn, J. Jacquot, M. Kubič, X. Litaudon, G. Lombard, O. Meyer, P. Mollard, K. Vulliez, RF-sheath patterns modification via novel Faraday screen and strap voltage imbalance on Tore Supra ion cyclotron antennae, Journal of Nuclear Materials 438 (2013) S330–S333, https://doi.org/10.1016/j.jnucmat.2013.01.061.

[74] the ASDEX Upgrade Team, Progress in controlling ICRF-edge interactions in ASDEX upgrade, 2015, p. 030004, https://doi.org/10.1063/1.4936469. http://aip.scitation.org/doi/abs/10.1063/1.4936469.California, USA

[75] V. Bobkov, D. Aguiam, R. Bilato, S. Brezinsek, L. Colas, H. Faugel, H. Fünfgelder, A. Herrmann, J. Jacquot, A. Kallenbach, D. Milanesio, R. Maggiora, R. Neu, J.-M. Noterdaeme, R. Ochoukov, S. Potzel, T. Pütterich, A. Silva, W. Tierens, A. Tuccilo, O. Tudisco, Y. Wang, Q. Yang, W. Zhang, ASDEX Upgrade Team and the EUROfusion MST1 Team, Making ICRF power compatible with a high-Z wall in ASDEX Upgrade, Plasma Physics and Controlled Fusion 59 (1) (2017) 014022, https://doi.org/10.1088/0741-3335/59/1/014022.

[76] V.L. Ginzburg, A.A. Ruhadze, Waves and Resonances in Magneto-active Plasma, in: S. Flügge, K. Rawer (Eds.), Geophysik III–VII volume 10 / 49 / 4, Springer Berlin Heidelberg, Berlin, Heidelberg, 1984, pp. 920–1085.Series Title: Encyclopedia of Physics / Handbuch der Physik

[77] E. Berro, E. Morales, Excitation of the lower-hybrid resonance at the plasma edge by ICRF couplers, IEEE Transactions on Plasma Science 18 (1) (1990) 142–148, https://doi.org/10.1109/27.45517.

[78] A. Messiaen, V. Maquet, Coaxial and surface mode excitation by an ICRF antenna in large machines like DEMO and ITER, Nuclear Fusion 60 (7) (2020) 076014, https://doi.org/10.1088/1741-4326/ab8d05.

[79] V. Bobkov, F. Braun, R. Dux, A. Herrmann, H. Faugel, H. Fünfgelder, A. Kallenbach, R. Neu, J.-M. Noterdaeme, R. Ochoukov, T. Pütterich, A. Tuccilo, O. Tudisco, Y. Wang, Q. Yang, ASDEX Upgrade team, First results with 3-strap ICRF antennas in ASDEX Upgrade, Nuclear Fusion 56 (8) (2016) 084001, https://doi.org/10.1088/0029-5515/56/8/084001.

[80] S. Wukitch, Y. Lin, J. Terry, M. Chilenski, T. Golfinopoulos, R. Hong, A. Hubbard, R. Mumgaard, R. Perkins, M. Reinke, G. Tynan, A.C.-M. Team, Towards ICRF antennas compatible with high performance plasmas: Characterization and mitigation of icrf antenna–plasma edge interaction. 22nd Topical Conference on Radio-Frequency Power in Plasmas, Aix-en-Provence, France, 2017, Technical Report, https://www1.psfc.mit.edu/research/alcator/pubs/RF/rf2017index_files/Wuktich_inv_RF2017.pdf.

[81] M. Usoltceva, R. Ochoukov, W. Tierens, A. Kostic, K. Crombé, S. Heuraux, J.-M. Noterdaeme, Simulation of the ion cyclotron range of frequencies slow wave and the lower hybrid resonance in 3D in RAPLICASOL, Plasma Physics and Controlled Fusion 61 (11) (2019) 115011, https://doi.org/10.1088/1361-6587/ab476d.

[82] A. Messiaen, V. Maquet, J. Ongena, Ion cyclotron resonance heating fast and slow wave excitation and power deposition in edge plasmas with application to ITER,

Plasma Physics and Controlled Fusion 63 (4) (2021) 045021, https://doi.org/10.1088/1361-6587/abdf2b.

[83] T. Jet, T. Teams, P.B.D.F.H. Start, ICRF results in D-T plasmas in JET and TFTR and implications for ITER, Plasma Physics and Controlled Fusion 40 (8A) (1998) A87–A103, https://doi.org/10.1088/0741-3335/40/8A/008.

[84] C.K. Phillips, M.G. Bell, R. Bell, N. Bretz, R.V. Budny, D.S. Darrow, B. Grek, G. Hammett, J.C. Hosea, H. Hsuan, D. Ignat, R. Majeski, E. Mazzucato, R. Nazikian, H. Park, J.H. Rogers, G. Schilling, J.E. Stevens, E. Synakowski, G. Taylor, J.R. Wilson, M.C. Zarnstorff, S.J. Zweben, C.E. Bush, R. Goldfinger, E. F. Jaeger, M. Murakami, D. Rasmussen, M. Bettenhausen, N.T. Lam, J. Scharer, R. Sund, O. Sauter, Ion cyclotron range of frequencies heating and current drive in deuterium–tritium plasmas, Physics of Plasmas 2 (6) (1995) 2427–2434, https://doi.org/10.1063/1.871266.

[85] J.R. Wilson, C.E. Bush, D. Darrow, J.C. Hosea, E.F. Jaeger, R. Majeski, M. Murakami, C.K. Phillips, J.H. Rogers, G. Schilling, J.E. Stevens, E. Synakowski, G. Taylor, Ion Cyclotron Range of Frequency Heating of a Deuterium-Tritium Plasma via the Second-Harmonic Tritium Cyclotron Resonance, Physical Review Letters 75 (5) (1995) 842–845, https://doi.org/10.1103/PhysRevLett.75.842.

[86] D. Van Eester, E. Lerche, R. Ragona, A. Messiaen, T. Wauters, JET contributors, Ion cyclotron resonance heating scenarios for DEMO, Nuclear Fusion 59 (10) (2019) 106051, https://doi.org/10.1088/1741-4326/ab318b.

[87] Y.O. Kazakov, J. Ongena, J.C. Wright, S.J. Wukitch, E. Lerche, M.J. Mantsinen, D. Van Eester, T. Craciunescu, V.G. Kiptily, Y. Lin, M. Nocente, F. Nabais, M.F. F. Nave, Y. Baranov, J. Bielecki, R. Bilato, V. Bobkov, K. Crombé, A. Czarnecka, J. M. Faustin, R. Felton, M. Fitzgerald, D. Gallart, L. Giacomelli, T. Golfinopoulos, A. E. Hubbard, P. Jacquet, T. Johnson, M. Lennholm, T. Loarer, M. Porkolab, S. E. Sharapov, D. Valcarcel, M. Van Schoor, H. Weisen, Efficient generation of energetic ions in multi-ion plasmas by radio-frequency heating, Nature Physics 13 (10) (2017) 973–978, https://doi.org/10.1038/nphys4167.

[88] J. Ongena, Y. Kazakov, Y. Baranov, C. Hellesen, J. Eriksson, T. Johnson, V. Kiptily, M. Mantsinen, M. Nocente, R. Bilato, A. Cardinali, C. Castaldo, K. Crombé, A. Czarnecka, R. Dumont, J. Faustin, L. Giacomelli, V. Goloborodko, J. Graves, P. Jacquet, N. Krawczyk, E. Lerche, L. Meneses, M. Nave, H. Patten, M. Schneider, D. Van Eester, H. Weisen, J. Wright, JET Contributors, Synergetic heating of D-NBI ions in the vicinity of the mode conversion layer in H-D plasmas in JET with the ITER like wall, EPJ Web of Conferences 157 (2017) 02006, https://doi.org/10.1051/epjconf/201715702006.

[89] Y.O. Kazakov, J. Ongena, J.C. Wright, S.J. Wukitch, V. Bobkov, J. Garcia, V. G. Kiptily, M.J. Mantsinen, M. Nocente, M. Schneider, H. Weisen, Y. Baranov, M. Baruzzo, R. Bilato, A. Chomiczewska, R. Coelho, T. Craciunescu, K. Crombé, M. Dreval, R. Dumont, P. Dumortier, F. Durodié, J. Eriksson, M. Fitzgerald, J. Galdon-Quiroga, D. Gallart, M. Garcia-Muñoz, L. Giacomelli, C. Giroud, J. Gonzalez-Martin, A. Hakola, P. Jacquet, T. Johnson, A. Kappatou, D. Keeling, D. King, K.K. Kirov, P. Lamalle, M. Lennholm, E. Lerche, M. Maslov, S. Mazzi, S. Menmuir, I. Monakhov, F. Nabais, M.F.F. Nave, R. Ochoukov, A.R. Polevoi, S. D. Pinches, U. Plank, D. Rigamonti, M. Salewski, P.A. Schneider, S.E. Sharapov, Ž. Štancar, A. Thorman, D. Valcarcel, D. Van Eester, M. Van Schoor, J. Varje, M. Weiland, N. Wendler, JET Contributors,, ASDEX Upgrade Team,, EUROfusion MST1 Team,, Alcator C-Mod Team, Physics and applications of three-ion ICRF scenarios for fusion research, Physics of Plasmas 28 (2) (2021) 020501, https://doi.org/10.1063/5.0021818.

[90] A. Di Siena, T. Görler, H. Doerk, E. Poli, R. Bilato, Fast-ion stabilization of tokamak plasma turbulence, Nuclear Fusion 58 (5) (2018) 054002, https://doi.org/10.1088/1741-4326/aaaf26.

[91] F.N. de Oliveira-Lopes, M.J. Mantsinen, Nonlinear electromagnetic stabilization of ITG microturbulence by fast ions in ASDEX Upgrade, 2021. Submitted to Nuclear Fusion.

[92] S. Mazzi, Towards enhanced performance in fusion plasmas via turbulence suppression by MeV ions, 2021. Submitted to Nature Physics.

[93] P. Vincenzi, P. Agostinetti, J.F. Artaud, T. Bolzonella, T. Kurki-Suonio, M. Mattei, M. Vallar, J. Varje, Optimization-oriented modelling of neutral beam injection for EU pulsed DEMO, Plasma Physics and Controlled Fusion 63 (6) (2021) 065014, https://doi.org/10.1088/1361-6587/abf402.

[94] P. Vincenzi, R. Ambrosino, J. Artaud, T. Bolzonella, L. Garzotti, G. Giruzzi, G. Granucci, F. Köchl, M. Mattei, M. Tran, R. Wenninger, EU DEMO transient phases: Main constraints and heating mix studies for ramp-up and ramp-down, Fusion Engineering and Design 123 (2017) 473–476, https://doi.org/10.1016/j.fusengdes.2017.02.064.

[95] G. Federici, C. Bachmann, W. Biel, L. Boccaccini, F. Cismondi, S. Ciattaglia, M. Coleman, C. Day, E. Diegele, T. Franke, M. Grattarola, H. Hurzlmeier, A. Ibarra, A. Loving, F. Maviglia, B. Meszaros, C. Morlock, M. Rieth, M. Shannon, N. Taylor, M.Q. Tran, J.H. You, R. Wenninger, L. Zani, Overview of the design approach and prioritization of R&D activities towards an EU DEMO, Fusion Engineering and Design 109-111 (2016) 1464–1474, https://doi.org/10.1016/j.fusengdes.2015.11.050.

[96] ITER Research Plan within the Staged Approach ITR 18-003 (2018), Technical Report, https://www.iter.org/doc/www/content/com/Lists/ITER TechnicalReports/Attachments/9/ITER-Research-Plan_final_ITR_FINAL-Cover_High-Res.pdf.

[97] P. Sonato, P. Agostinetti, T. Bolzonella, F. Cismondi, U. Fantz, A. Fassina, T. Franke, I. Furno, C. Hopf, I. Jenkins, E. Sartori, M.Q. Tran, J. Varje, P. Vincenzi, L. Zanotto, Conceptual design of the DEMO neutral beam injectors: main developments and R&D achievements, Nuclear Fusion 57 (5) (2017) 056026, https://doi.org/10.1088/1741-4326/aa6186.Publisher: IOP Publishing

[98] G. Serianni, V. Toigo, M. Bigi, M. Boldrin, G. Chitarin, S. Dal Bello, L. Grando, A. Luchetta, D. Marcuzzi, R. Pasqualotto, N. Pomaro, P. Zaccaria, L. Zanotto, P. Agostinetti, M. Agostini, V. Antoni, D. Aprile, M. Barbisan, M. Battistella, M. Brombin, A. Canton, R. Cavazzana, M. Dalla Palma, M. Dan, R. Delogu, A. De Lorenzi, M. De Muri, S. Denizeau, M. Fadone, F. Fellin, A. Ferro, E. Gaio, G. Gambetta, F. Gasparini, F. Gnesotto, P. Jain, A. Maistrello, G. Manduchi, S. Manfrin, G. Marchiori, N. Marconato, M. Moresco, T. Patton, M. Pavei, S. Peruzzo, N. Pilan, A. Pimazzoni, R. Piovan, C. Poggi, M. Recchia, A. Rigoni, A. Rizzolo, G. Rostagni, E. Sartori, M. Siragusa, P. Sonato, E. Spada, S. Spagnolo, M. Spolaore, C. Taliercio, P. Tinti, M. Ugoletti, M. Valente, A. Zamengo, B. Zaniol, M. Zaupa, M. Cavenago, D. Boilson, C. Rotti, P. Veltri, J. Chareyre, H. Decamps, M. Dremel, J. Graceffa, F. Geli, B. Schunke, L. Svensson, M. Urbani, T. Bonicelli, G. Agarici, A. Garbuglia, A. Masiello, F. Paolucci, M. Simon, L. Bailly-Maitre, E. Bragulat, G. Gomez, D. Gutierrez, C. Labate, G. Mico, J.F. Moreno, V. Pilard, G. Kouzmenko, A. Rousseau, A. Chakraborty, U. Baruah, H. Patel, N.P. Singh, A. Patel, H. Dhola, B. Raval, S. Cristofaro, U. Fantz, B. Heinemann, W. Kraus, M. Kashiwagi, H. Tobari, First operation in SPIDER and the path to complete MITICA, Review of Scientific Instruments 91 (2) (2020) 023510, https://doi.org/10.1063/1.5133076.Publisher: American Institute of Physics

[99] B. Heinemann, U. Fantz, W. Kraus, D. Wünderlich, F. Bonomo, M. Froeschle, I. Mario, R. Nocentini, R. Riedl, C. Wimmer, Latest achievements of the negative ion beam test facility ELISE, Fusion Engineering and Design 136 (2018) 569–574, https://doi.org/10.1016/j.fusengdes.2018.03.025.

[100] E. Surrey, A. Holmes, The beam driven plasma neutralizer, AIP Conference Proceedings 1515 (1) (2013) 532–540, https://doi.org/10.1063/1.4792825. Publisher: American Institute of Physics

[101] U. Fantz, C. Hopf, R. Friedl, S. Cristofaro, B. Heinemann, S. Lishev, A. Mimo, Technology developments for a beam source of an NNBI system for DEMO, Fusion Engineering and Design 136 (2018) 340–344, https://doi.org/10.1016/j.fusengdes.2018.02.025.

[102] C. Hopf, G. Starnella, N. den Harder, B. Heinemann, U. Fantz, A conceptual system design study for an NBI beamline for the European DEMO, Fusion Engineering and Design 146 (2019) 705–708, https://doi.org/10.1016/j.fusengdes.2019.01.060.

[103] P. Agostinetti, T. Franke, U. Fantz, C. Hopf, N. Mantel, M.Q. Tran, RAMI evaluation of the beam source for the DEMO neutral beam injectors, Fusion Engineering and Design 159 (2020) 111628, https://doi.org/10.1016/j.fusengdes.2020.111628.

[104] D. Marcuzzi, P. Agostinetti, M. Dalla Palma, M. De Muri, G. Chitarin, G. Gambetta, N. Marconato, R. Pasqualotto, M. Pavei, N. Pilan, A. Rizzolo, G. Serianni, V. Toigo, L. Trevisan, M. Visentin, P. Zaccaria, M. Zaupa, D. Boilson, J. Graceffa, R.S. Hemsworth, C.H. Choi, M. Marti, K. Roux, M.J. Singh, A. Masiello, M. Froeschle, B. Heinemann, R. Nocentini, R. Riedl, H. Tobari, H.P. L. de Esch, V.N. Muvvala, Final design of the beam source for the MITICA injector, Review of Scientific Instruments 87 (2) (2015) 02B309, https://doi.org/10.1063/1.4932615.Publisher: American Institute of Physics

[105] D. Zielke, S. Briefi, U. Fantz, RF power transfer efficiency and plasma parameters of low pressure high power ICPs, Journal of Physics D: Applied Physics 54 (15) (2021) 155202, https://doi.org/10.1088/1361-6463/abd8ee.Publisher: IOP Publishing

[106] P. Agostinetti, S. Hanke, H. Strobel, X. Luo, F. Veronese, Report on NB Injector and System Concept 2020, Technical Report EFDA_D_2NTBNF, http://idm.euro-fusion.org/?uid=2NTBNF.

[107] M.J. Singh, D. Boilson, R.S. Hemsworth, F. Geli, J. Graceffa, M. Urbani, E. Dlougach, A. Krylov, B. Schunke, J. Chareyre, Powerloads on the front end components and the duct of the heating and diagnostic neutral beam lines at ITER, 2015, p. 050011, https://doi.org/10.1063/1.4916468. http://aip.scitation.org/doi/abs/10.1063/1.4916468.Garching, Germany

[108] E. Speth, H.D. Falter, P. Franzen, U. Fantz, M. Bandyopadhyay, S. Christ, A. Encheva, M. Fröschle, D. Holtum, B. Heinemann, W. Kraus, A. Lorenz, C. Martens, P. McNeely, S. Obermayer, R. Riedl, R. Süss, A. Tanga, R. Wilhelm, D. Wünderlich, Overview of the RF source development programme at IPP Garching, Nuclear Fusion 46 (6) (2006) S220–S238, https://doi.org/10.1088/0029-5515/46/6/S03.Publisher: IOP Publishing

[109] R. Hemsworth, H. Decamps, J. Graceffa, B. Schunke, M. Tanaka, M. Dremel, A. Tanga, H.P.L.D. Esch, F. Geli, J. Milnes, T. Inoue, D. Marcuzzi, P. Sonato, P. Zaccaria, Status of the ITER heating neutral beam system, Nuclear Fusion 49 (4) (2009) 045006, https://doi.org/10.1088/0029-5515/49/4/045006. Publisher: IOP Publishing

[110] U. Fantz, C. Hopf, D. Wünderlich, R. Friedl, M. Fröschle, B. Heinemann, W. Kraus, U. Kurutz, R. Riedl, R. Nocentini, L. Schiesko, Towards powerful negative ion beams at the test facility ELISE for the ITER and DEMO NBI systems, Nuclear Fusion 57 (11) (2017) 116007, https://doi.org/10.1088/1741-4326/aa778b. Publisher: IOP Publishing

[111] A. Simonin, R. Agnello, S. Bechu, J.M. Bernard, C. Blondel, J.P. Boeuf, D. Bresteau, G. Cartry, W. Chaibi, C. Drag, B.P. Duval, H.P.L.d. Esch, G. Fubiani, I. Furno, C. Grand, P. Guittienne, A. Howling, R. Jacquier, C. Marini, I. Morgal, Negative ion source development for a photoneutralization based neutral beam system for future fusion reactors, New Journal of Physics 18 (12) (2016) 125005, https://doi.org/10.1088/1367-2630/18/12/125005.Publisher: IOP Publishing

[112] C. Wimmer, U. Fantz, E. Aza, J. Jovović, W. Kraus, A. Mimo, L. Schiesko, Investigation of plasma parameters at BATMAN for variation of the Cs evaporation asymmetry and comparing two driver geometries, AIP Conference Proceedings 1869 (1) (2017) 030021, https://doi.org/10.1063/1.4995741. Publisher: American Institute of Physics

[113] A. Mimo, C. Wimmer, D. Wünderlich, U. Fantz, Studies of Cs dynamics in large ion sources using the CsFlow3D code, AIP Conference Proceedings 2052 (1)

(2018) 040009, https://doi.org/10.1063/1.5083743.Publisher: American Institute of Physics

[114] D. Wünderlich, Contribution to FEC Conference, 2021. Submitted to Nuclear Fusion.

[115] K.H. Berkner, R.V. Pyle, S.E. Savas, K.R. Stalder, Plasma neutralizers for H/sup -/ or D/sup -/ beams. Technical Report, California Univ., Berkeley (USA). Lawrence Berkeley Lab., 1980.

[116] I. Turner, A.J.T. Holmes, Model for a beam driven plasma neutraliser based on ITER beam geometry, Fusion Engineering and Design 149 (2019) 111327, https://doi.org/10.1016/j.fusengdes.2019.111327.

[117] A. Pimazzoni, E. Sartori, G. Serianni, On the role of dissociative recombination on the effectiveness of a plasma neutralizer in DEMO fusion plant, Fusion Engineering and Design 171 (2021) 112693, https://doi.org/10.1016/j.fusengdes.2021.112693.

[118] G. Starnella, C. Hopf and P. Maya, On suitable experiments for demonstrating the feasibility of the beam-driven plasma neutraliser for neutral beam injectors for reactor-class fusion devices, 2021. Submitted.

[119] R. McAdams, A.J.T. Holmes, M. Porton, A. Benn, E. Surrey, T.T.C. Jones, Advanced energy recovery concepts for negative ion beamlines in fusion power plants, AIP Conference Proceedings 1515 (1) (2013) 559–568, https://doi.org/10.1063/1.4792828.Publisher: American Institute of Physics

[120] J. Pamela, S. Laffite, Conceptual study of a purely electrostatic energy recovery system for negative-ion-based neutral beam injectors, Nuclear Instruments and Methods in Physics Research Section A: Accelerators, Spectrometers, Detectors and Associated Equipment 295 (3) (1990) 453–460, https://doi.org/10.1016/0168-9002(90)90726-M.

[121] V. Variale, M. Cavenago, B. Skarbo, V. Valentino, Secondary electrons problem study in beam energy recovery for fusion: Experimental apparatus, AIP Conference Proceedings 2052 (1) (2018) 070006, https://doi.org/10.1063/1.5083786.Publisher: American Institute of Physics

[122] T. Inoue, M. Hanada, M. Kashiwagi, S. Nishio, K. Sakamoto, M. Sato, M. Taniguchi, K. Tobita, K. Watanabe, Design study of a neutral beam injector for fusion DEMO plant at JAERI, Fusion Engineering and Design 81 (8) (2006) 1291–1297, https://doi.org/10.1016/j.fusengdes.2005.08.074.

[123] M. Kovari, B. Crowley, Laser photodetachment neutraliser for negative ion beams, Fusion Engineering and Design 85 (5) (2010) 745–751, https://doi.org/10.1016/j.fusengdes.2010.04.055.

[124] A. Simonin, C. Blondel, W. Chaibi, C. Dechelle, C. Drag, E. Villedieu, Towards a maintainable and high efficiency neutral beam system for future fusion reactors, Nuclear Fusion 61 (4) (2021) 046003, https://doi.org/10.1088/1741-4326/abdac2.Publisher: IOP Publishing

[125] D. Fiorucci, J. Feng, M. Pichot, W. Chaibi, Thermal effects in high power cavities for photoneutralization of Dbeams in future neutral beam injectors, AIP Conference Proceedings 1655 (1) (2015) 050010, https://doi.org/10.1063/1.4916467.Publisher: American Institute of Physics

[126] H. Kreckel, H. Bruhns, M. Čížek, S.C.O. Glover, K.A. Miller, X. Urbain, D.W. Savin, Experimental Results for H2 Formation from Hand H and Implications for First Star Formation, Science 329 (5987) (2010) 69–71, https://doi.org/10.1126/science.1187191.Publisher: American Association for the Advancement of Science Section: Report

[127] S.S. Popov, M.G. Atlukhanov, A.V. Burdakov, A.A. Ivanov, A.A. Kasatov, A. V. Kolmogorov, R.V. Vakhrushev, M.Y. Ushkova, A. Smirnov, A. Dunaevsky, Neutralization of negative hydrogen and deuterium ion beams using non-resonance adiabatic photon trap, Nuclear Fusion 58 (9) (2018) 096016, https://doi.org/10.1088/1741-4326/aacb02.Publisher: IOP Publishing

[128] A. Fassina, D. Fiorucci, L. Giudicotti, P. Vincenzi, Performance analysis and application study of a laser enhancement cavity for photo-neutralization of Negative Ion Beams, Journal of Instrumentation 15 (02) (2020), https://doi.org/10.1088/1748-0221/15/02/C02031.C02031–C02031

[129] W. Chaibi, C. Blondel, L. Cabaret, C. Delsart, C. Drag, A. Simonin, Photoneutralization of Negative Ion Beam for Future Fusion Reactor, AIP Conference Proceedings 1097 (1) (2009) 385–394, https://doi.org/10.1063/1.3112535.Publisher: American Institute of Physics

[130] D. Bresteau, C. Blondel, C. Drag, Saturation of the photoneutralization of a H beam in continuous operation, Review of Scientific Instruments 88 (11) (2017) 113103, https://doi.org/10.1063/1.4995390.Publisher: American Institute of Physics

[131] R. Friedl, F. Merk, C. Hopf, U. Fantz, Laboratory experiment for the development of a laser neutralizer in view of DEMO NNBI, AIP Conference Proceedings 2011 (1) (2018) 060006, https://doi.org/10.1063/1.5053335.Publisher: American Institute of Physics

[132] D. Martynov, E. Hall, B. Abbott, R. Abbott, T. Abbott, C. Adams, R. Adhikari, R. Anderson, S. Anderson, K. Arai, M. Arain, S. Aston, L. Austin, S. Ballmer, M. Barbet, D. Barker, B. Barr, L. Barsotti, J. Bartlett, M. Barton, I. Bartos, J. Batch, A. Bell, I. Belopolski, J. Bergman, J. Betzwieser, G. Billingsley, J. Birch, S. Biscans, C. Biwer, E. Black, C. Blair, C. Bogan, C. Bond, R. Bork, D. Bridges, A. Brooks, D. Brown, L. Carbone, C. Celerier, G. Ciani, F. Clara, D. Cook, S. Countryman, M. Cowart, D. Coyne, A. Cumming, L. Cunningham, M. Damjanic, R. Dannenberg, K. Danzmann, C.D.S. Costa, E. Daw, D. DeBra, R. DeRosa, R. DeSalvo, K. Dooley, S. Doravari, J. Driggers, S. Dwyer, A. Effler, T. Etzel, M. Evans, T. Evans, M. Factourovich, H. Fair, D. Feldbaum, R. Fisher, S. Foley, M. Frede, A. Freise, P. Fritschel, V. Frolov, P. Fulda, M. Fyffe, V. Galdi, J. Giaime, K. Giardina, J. Gleason, R. Goetz, S. Gras, C. Gray, R. Greenhalgh, H. Grote, C. Guido, K. Gushwa, E. Gustafson, R. Gustafson, G. Hammond, J. Hanks, J. Hanson, T. Hardwick, G. Harry, K. Haughian, J. Heefner, M. Heintze, A. Heptonstall, D. Hoak, J. Hough, A. Ivanov, K. Izumi, M. Jacobson, E. James, R. Jones, S. Kandhasamy, S. Karki, M. Kasprzack, S. Kaufer, K. Kawabe, W. Kells, N. Kijbunchoo, E. King, P. King, D. Kinzel, J. Kissel, K. Kokeyama, W. Korth, G. Kuehn, P. Kwee, M. Landry, B. Lantz, A. Le Roux, B. Levine, J. Lewis, V. Lhuillier, N. Lockerbie, M. Lormand, M. Lubinski, A. Lundgren, T. MacDonald, M. MacInnis, D. Macleod, M. Mageswaran, K. Mailand, S. Márka, Z. Márka, A. Markosyan, E. Maros, I. Martin, R. Martin, J. Marx, K. Mason, T. Massinger, F. Matichard, N. Mavalvala, R. McCarthy, D. McClelland, S. McCormick, G. McIntyre, J. McIver, E. Merilh, M. Meyer, P. Meyers, J. Miller, R. Mittleman, G. Moreno, C. Mueller, G. Mueller, A. Mullavey, J. Munch, P. Murray, L. Nuttall, J. Oberling, J. O'Dell, P. Oppermann, R.J. Oram, B. O'Reilly, C. Osthelder, D. Ottaway, H. Overmier, J. Palamos, H. Paris, W. Parker, Z. Patrick, A. Pele, S. Penn, M. Phelps, M. Pickenpack, V. Pierro, I. Pinto, J. Poeld, M. Principe, L. Prokhorov, O. Puncken, V. Quetschke, E. Quintero, F. Raab, H. Radkins, P. Raffai, C. Ramet, C. Reed, S. Reid, D. Reitze, N. Robertson, J. Rollins, V. Roma, J. Romie, S. Rowan, K. Ryan, T. Sadecki, E. Sanchez, V. Sandberg, V. Sannibale, R. Savage, R. Schofield, B. Schultz, P. Schwinberg, D. Sellers, A. Sevigny, D. Shaddock, Z. Shao, B. Shapiro, P. Shawhan, D. Shoemaker, D. Sigg, B. Slagmolen, J. Smith, M. Smith, N. Smith-Lefebvre, B. Sorazu, A. Staley, A. Stein, A. Stochino, K. Strain, R. Taylor, M. Thomas, P. Thomas, K. Thorne, E. Thrane, K. Tokmakov, C. Torrie, G. Traylor, G. Vajente, G. Valdes, A. van Veggel, M. Vargas, A. Vecchio, P. Veitch, K. Venkateswara, T. Vo, C. Vorvick, S. Waldman, M. Walker, R. Ward, J. Warner, B. Weaver, R. Weiss, T. Welborn, P. Weßels, C. Wilkinson, P. Willems, L. Williams, B. Willke, I. Wilmut, L. Winkelmann, C. Wipf, J. Worden, G. Wu, H. Yamamoto, C. Yancey, H. Yu, L. Zhang, M. Zucker, J. Zweizig, Sensitivity of the Advanced LIGO detectors at the beginning of gravitational wave astronomy, Physical Review D 93 (11) (2016) 112004, https://doi.org/10.1103/PhysRevD.93.112004.Publisher: American Physical Society

[133] R.W.P. Drever, J.L. Hall, F.V. Kowalski, J. Hough, G.M. Ford, A.J. Munley, H. Ward, Laser phase and frequency stabilization using an optical resonator, Applied Physics B 31 (2) (1983) 97–105, https://doi.org/10.1007/BF00702605.

[134] D. Fiorucci, A. Hreibi, W. Chaibi, Telescope-based cavity for negative ion beam neutralization in future fusion reactors, Applied Optics 57 (7) (2018) B122–B134, https://doi.org/10.1364/AO.57.00B122.Publisher: Optical Society of America

[135] R.S. Hemsworth, D. Boilson, P. Blatchford, M.D. Palma, G. Chitarin, H.P.L. de Esch, F. Geli, M. Dremel, J. Graceffa, D. Marcuzzi, G. Serianni, D. Shah, M. Singh, M. Urbani, P. Zaccaria, Overview of the design of the ITER heating neutral beam injectors, New Journal of Physics 19 (2) (2017) 025005, https://doi.org/10.1088/1367-2630/19/2/025005.